PCCP

PERSPECTIVE

View Article Online
View Journal | View Issue

Check for updates

Cite this: *Phys. Chem. Chem. Phys.*, 2019, **21**, 12067

Received 19th April 2019,
Accepted 23rd May 2019

DOI: 10.1039/c9cp02225b

rsc.li/pccp

Vibrational sum-frequency generation spectroscopy of electrode surfaces: studying the mechanisms of sustainable fuel generation and utilisation

Adrian M. Gardner, Khezar H. Saeed and Alexander J. Cowan *

The electrocatalytic oxidation of water coupled to the reduction of carbon dioxide, to make carbon based products, or the reduction of protons to provide hydrogen, offers a sustainable route to generating useful fuels. However new improved electrocatalysts and electrode materials are needed for these reactions. Similarly fuel cells for fuel utilisation rely on precious metal electrodes and new lower-cost materials are needed. Developing efficient catalysts for sustainable fuel generation can be accelerated with an improved understanding of the underlying mechanisms. Herein, we present a perspective on the use of vibrational sum-frequency generation (VSFG) spectroscopy to study such electrocatalytic mechanisms. We briefly outline the basic principles of VSFG spectroscopy pertinent to the study of electrochemical interfaces. We then review the use of VSFG to study water at charged and electrode interfaces, relevant to the mechanisms of water oxidation, the mechanisms of alcohol oxidation and also molecular electrocatalysts for carbon dioxide reduction.

1 Introduction

Electrochemical water splitting and CO_2 reduction are key processes for driving the production of high energy density fuel from abundant or waste resources.[1,2] Electrolysers, such as the one depicted in Fig. 1(a), can oxidise water and reduce CO_2 to form a variety of chemicals and fuels. The simplest product of this process is a mixture of CO and H_2 (syngas) which can undergo well-established Fischer–Tropsch-based chemistry to form conventional hydrocarbon fuels that can be fed into existing infrastructure.[3] Alternatively, the selectivity of the overall reaction can be tuned to target small organic molecules such as formic acid, methanol or ethanol, which can then drive the reverse electrochemical reaction in a fuel cell to directly generate electricity. However, the current catalysts and electrodes for both use in electrolysers and fuel cells are either prohibitively expensive, fail during prolonged used or operate with low efficiencies. Therefore, intense research is underway with the aim of delivering scalable materials with improved efficiencies during fuel generation and utilisation.

The development of new electrocatalysts and electrodes can be accelerated through an improved understanding of the underlying mechanistic details and failings of the current state-of-the-art materials. However, mechanistic studies of electrode surfaces are challenging due to the low concentrations of often short-lived species at an electrode surface, the spectral features of which can be masked by the strong signal from the bulk electrolyte. Surface-sensitive spectroscopies are therefore vital in understanding the mechanisms that take place at the electrochemical interface. There is a long history of utilising surface enhanced vibrational spectroscopies, such as surface enhanced Raman spectroscopy, SERS and surface enhanced infrared absorption spectroscopy, SEIRAS, in order to study electrochemical reactions.[4,5] This perspective presents VSFG as an alternative, surface-specific, vibrational spectroscopy as a probe of the electrochemical interface. Following a brief summary of the principles of VSFG we review the application of VSFG to three specific fuel generation (water oxidation, carbon dioxide reduction) and utilisation (alcohol oxidation) electrocatalytic mechanisms.

1.1. VSFG technique/principles

The principles of VSFG spectroscopy have been described in detail elsewhere[6,7] and here we only reiterate the most pertinent points to this application-based perspective. In the most simple model VSFG can be thought of as a resonant vibrational transition, driven by absorption of an infra-red photon, followed by Raman scattering of a visible (or near infra-red, but historically referred to as ''visible'') photon. When anti-Stokes scattering occurs a photon which has a frequency that is the sum of the IR and visible photons is

---

Stephenson Institute for Renewable Energy and the Department of Chemistry, University of Liverpool, Liverpool, L69 7ZD, UK. E-mail: acowan@liverpool.ac.uk

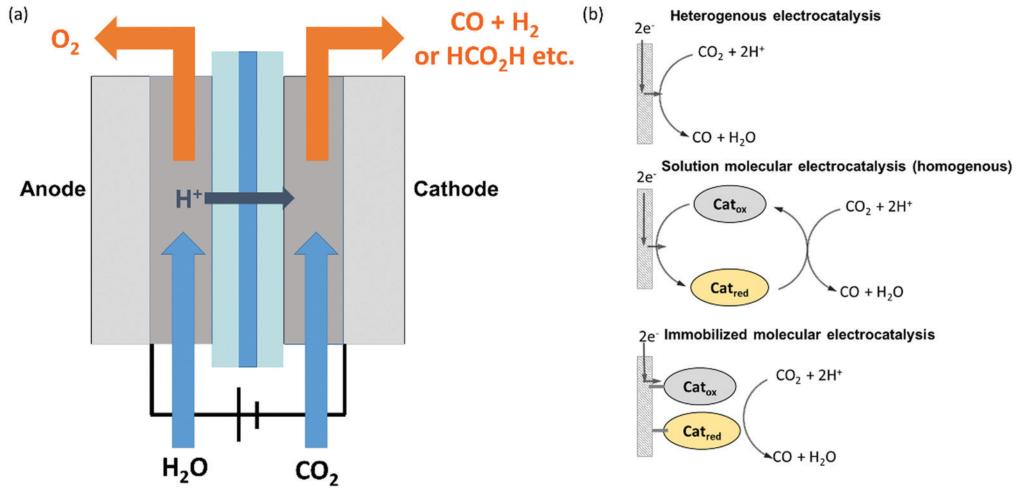

Fig. 1 Schematic of (a) a CO_2 electrolyser with water as the proton source and (b) electrocatalysis can occur with the electrode surface itself playing a catalytic role (top), with a molecular catalyst in solution (middle) or through a molecular catalyst that is immobilized onto the non-catalytic electrode support to facilitate electron transfer (bottom).

produced; it is this sum-frequency photon that is subsequently detected, eqn (1).

$$\omega_{\mathrm{SFG}} = \omega_{\mathrm{IR}} + \omega_{\mathrm{vis}} \tag{1}$$

In principle, the measurement of photons of higher frequency allows background-free detection, enabling even single photons to be detected. Furthermore, inference that a resonant vibrational transition has taken place arises from detection of the, typically visible, sum-frequency photon. Compared to IR detectors visible light detectors have higher quantum efficiencies, are inexpensive and readily available.

To be observed in VSFG spectroscopy the resonant vibrational transition is required to be both IR and Raman active. VSFG is a second order non-linear process, which, in the electric dipole approximation, is forbidden in bulk centrosymmetric environments; however, when two centrosymmetric bulk substances are brought together, the inversion symmetry is inherently broken at the interface between the two. This gives rise to the surface specificity of VSFG spectroscopy: the sum-frequency photon can only be generated by molecules which reside at the interface between these two centrosymmetric environments. The intensity of the resulting resonant VSFG signal is related to the resonant polarization of the molecules at the interface, which in turn, results from the oscillating electric dipole of the vibrating molecule. With the appropriate experimental design, discussed in detail below in Section 1.1., surface VSFG spectra can be recorded with sub-monolayer sensitivity outside of the UHV conditions typically required for surface-sensitive photoelectron spectroscopies. Furthermore, VSFG can be applied to a wide range of electrode materials, avoiding the need for the surface roughening treatments used in surface enhanced IR absorption spectroscopy and surfaced enhanced Raman spectroscopy.

A complication to VSFG spectroscopy occurs through the observance of a non-resonant (NR) sum-frequency signal generated at the interface. Typically, large NR signals are observed when studying metallic surfaces, as is the case for many electrochemical systems. The intensity of the NR-SFG field is largely independent of the frequency of the IR pulse and can be thought of as a transition to a virtual state driven by the IR pulse, followed by scattering of the visible (or NIR) pulse *via* a second virtual state. The net non-resonant polarization is a result of the response of the electrons at the surface to the presence of the intense laser fields. In the absence of an applied large static electric field the intensity of the resulting VSFG signal is dependent on the polarizability of the species present at the surface:

$$\begin{aligned} I_{\mathrm{VSFG}}(\omega) \propto |P_{\mathrm{VSFG}}(\omega)|^2 &= (|\chi^{(2)}_{\mathrm{eff}}(\omega)|E_{\mathrm{IR}}E_{\mathrm{vis}})^2 \\ &= (|\chi^{(2)}_{\mathrm{NR}}(\omega) + \chi^{(2)}_{\mathrm{R}}(\omega)|E_{\mathrm{IR}}E_{\mathrm{vis}})^2 \end{aligned} \tag{2}$$

where $I_{\mathrm{VSFG}}(\omega)$ and $P_{\mathrm{VSFG}}(\omega)$ are the frequency dependent VSFG intensity and net polarization, respectively; $\chi^{(2)}_{\mathrm{eff}}(\omega)$ is the frequency dependent macroscopic effective second-order nonlinear susceptibility of the interface, which can be separated into $\chi^{(2)}_{\mathrm{NR}}(\omega)$ and $\chi^{(2)}_{\mathrm{R}}(\omega)$ contributions which are the frequency dependent second-order non-resonant and resonant nonlinear susceptibilities, respectively. E_{IR} and E_{vis} are the intensities of the IR and "visible" electric fields, respectively. The intensity of the reflected and transmitted VSFG signal is dependent on the Fresnel factors governing the interaction of the VSFG beam with the interface; the reader is referred to recent studies[8–13] for a full description of this, however we note that understanding the frequency dependence of the Fresnel factors is often crucial to understand observed VSFG spectra and becomes increasing complicated and important when multiple interfaces are present.[14,15]

The second order nonlinear susceptibility has both real and imaginary parts therefore the overall VSFG signal is dependent on the relative phase of both $\chi^{(2)}_{\mathrm{NR}}(\omega)$ and $\chi^{(2)}_{\mathrm{R}}(\omega)$. This results in more complicated spectra being obtained than in linear spectroscopy where the intensities of overlapping features are purely additive. Instead, dependent on the relative phases, resonant signals may interfere constructively or destructively with the non-resonant signal appearing as peaks or dips in the ω_{IR} independent background. This is also true in the case where two resonant vibrations overlap in frequency. Owing to this, analysis of VSFG spectra requires careful deconvolution. This is typically performed by fitting the observed $I_{\mathrm{VSFG}}(\omega)$, which is proportional to $\chi^{(2)}_{\mathrm{eff}}(\omega)$ to eqn (3):

$$\chi^{(2)}_{\mathrm{eff}}(\omega) = \chi^{(2)}_{\mathrm{NR}}(\omega) + \sum_q \frac{A_q}{\omega_2 - \omega_q + i\Gamma_q} \tag{3}$$

where A_q is the amplitude of vibrational mode q, at a centre frequency, ω_q, with a damping constant Γ_q, typically in the form of a Lorentzian distribution.

The macroscopic resonant nonlinear susceptibility, $\chi^{(2)}_{\mathrm{R}}$, is related to the molecular hyperpolarizability, $\beta^{(2)}$, averaged over the orientational molecular distribution at the interface, as described by eqn (4). This relationship requires that in order to observe a resonant VSFG response, the molecules at the surface must be ordered. Furthermore, the intensity of the resonant VSFG signal, $I_{\mathrm{(R)VSFG}}$, scales quadratically with the number density of molecules, N, limiting the sensitivity of VSFG spectroscopy.

$$I_{\mathrm{(R)VSFG}}(\omega) \propto (|\chi^{(2)}_{\mathrm{R}}(\omega)|)^2 = N^2|\langle\beta^{(2)}\rangle|^2 \tag{4}$$

Employing different polarizations of input and output radiation allows different tensors of $\chi^{(2)}_{\mathrm{eff}}$ to be probed, from which molecular orientation can be inferred. This is beyond the scope of this article, and the reader is referred to the tutorial review of Lambert and Davies[16] to learn more about this effect.

In reality during VSFG studies of molecules at the electrode–electrolyte interface under applied potential (φ) may also experience large static electric fields (E_{DC}), which can interact with the intense electric field of the IR and "visible" laser pulses inducing a net polarization throughout the double layer, which is dependent on the third order non-linear susceptibility, $\chi^{(3)}_{\mathrm{eff}}$, eqn (5).

$$P_{\mathrm{VSFG}}(\omega,\varphi) \propto \chi^{(2)}_{\mathrm{eff}}(\omega)E_{\mathrm{IR}}E_{\mathrm{vis}} + \chi^{(3)}_{\mathrm{eff}}(\omega)E_{\mathrm{IR}}E_{\mathrm{vis}}E_{\mathrm{DC}} \tag{5}$$

The presence of the third order term results in production of radiation at the sum frequency, which interacts constructively or destructively with the VSFG radiation (which arises owing to the $\chi^{(2)}_{\mathrm{eff}}$ term), depending on their relative phases, which cannot be determined *a priori*. In this perspective we will discuss third order contributions where appropriate. For a thorough analysis of the information which can be untangled from potential dependent non-resonant signal, the reader is directed to the excellent perspective of García Rey and Dlott.[17]

1.2. Experiment design for *in situ* VSFG spectroscopy of electrodes

Early studies employing VSFG spectroscopy were hampered by the difficulty in generating intense, tuneable, IR laser fields. In early laboratory-based experiments, low power, low repetition rate lasers, typically 10 Hz, were employed, although the earliest VSFG study was achieved using a CO_2 laser with a repetition rate of 0.5 Hz.[18] The first potential dependent VSFG study took advantage of the significantly higher power obtained using a free-electron laser source.[19] Despite these differences, one common theme of these studies is the relatively narrow linewidth of the IR radiation employed, typically $<10\ \mathrm{cm}^{-1}$. The IR and "visible" laser beams were focused and overlapped (spatially and temporally) at the sample interface; the reflected VSFG beam was detected using standard photon counting techniques, Fig. 2(a).

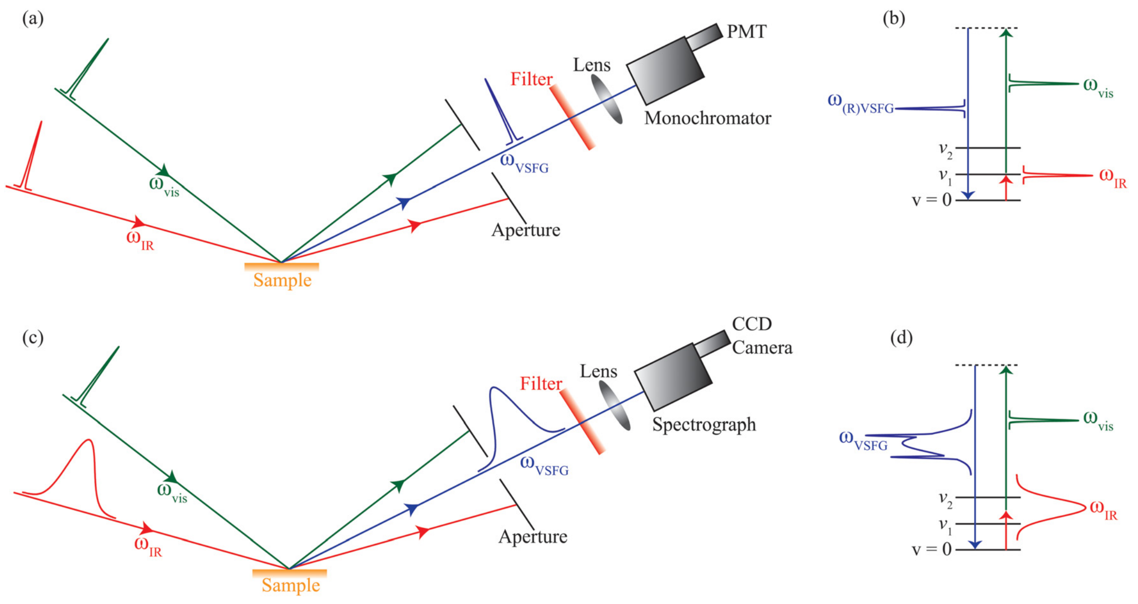

Fig. 2 VSFG experimental designs using: (a) narrowband (>1 ps) IR pulses, where the spectra are collected by scanning across the IR frequencies; (b) Resonant VSFG response, $\omega_{\mathrm{(R)VSFG}}$, is only observed when ωIR is coincident with an allowed vibrational transition; or (c) using broadband (≤100's fs) IR pulses imaging a broad range of IR frequencies in a single shot, where (d) ω_{VSFG} is observed for all allowed vibrational transitions encompassed by the broadband IR radiation, along with a NR component which follows the intensity profile of ω_{IR}. Based on Fig. 5 from ref. 45.

The resulting VSFG reflection is coherent and occurs at a well defined angle, which is dependent on the angle of incidence of the IR and "visible" input beams, allowing efficient spatial and spectral filtering of the VSFG beam from the input beams. The intensity of the VSFG signal was recorded as a function of IR frequency as the output of the IR light source was scanned, resulting in the VSFG spectrum being obtained, Fig. 2(a). These early narrowband studies paved the way for "high-resolution" VSFG spectroscopy performed in recent years. It is now even possible to purchase a commercial VSFG spectrometer which employ lasers with a pulse width of 10's ps, and linewidths of <2 cm^{-1}.

Stephenson and coworkers proposed the use of a broadband (250 cm^{-1}) IR laser with a pulse duration of $\sim$220 fs, combined with a narrowband "visible" ($\sim$795 nm) laser pulse with varying linewidths between 2.5 and 20 cm^{-1}, which may be termed broadband vibrational sum-frequency generation, BB-VSFG, spectroscopy.[20] The resulting VSFG radiation was collected, dispersed by a spectrograph and detected by a CCD camera, Fig. 2(c). A broad nonresonant background signal was observed, with an intensity distribution which followed the spectral profile of the broadband IR pulse, with resonant bands superimposed within this background. The use of lasers with pulse durations of 100's fs, in principle, allows for high repetition ($>$1 kHz) pump lasers to be employed; this, combined with the removal of the requirement for the IR frequency to be scanned, decreases acquisition times greatly and this has led to BB-VSFG being extensively applied to the study of electrode surfaces.[21] However, the current availability of chemically stable window materials with sufficient transparency in the far IR complicates the use of *in situ* electrochemical VSFG for the detection of vibrational frequencies below 700 cm^{-1}, a region which can readily be probed using various surface-enhanced Raman spectroscopies.

Using the principles of BB-VSFG spectroscopy, Dlott and coworkers proposed the use of a Fabry–Perot etalon to produce a time asymmetric (fast rising onset with an exponential tail), narrowband (5 to 15 cm^{-1}), "visible" (800 nm) pulse, which allowed effective suppression of the NR signal, whilst providing a minor perturbation to that of resonant vibrations.[22] The NR response of the interface is short lived, and is typically only observed when the IR and "visible" pulses are simultaneously present at the sample interface. It was shown that when a delay between the IR and "visible" pulse of greater than the IR pulse duration was introduced, little, to no, NR signal was detected.[21] The resonant VSFG response would be expected to be attenuated by a factor of $\sim(1 - t_p/T_2)$ where t_p is the IR pulse duration and T_2 is the vibrational dephasing time; the principle of this method is shown in Fig. 3(a). However, this method of NR suppression becomes problematic when t_p and T_2 become similar. Both Dlott's group,[17] and our own,[23–25] have employed this non-resonant suppression BB-VSFG technique to study species under potential control. A typical spectrometer employed in these studies is shown in Fig. 3(b).

Shen and coworkers pioneered the technique of Phase Sensitive Vibrational Sum Frequency Generation, PS-VSFG, spectroscopy, which allows determination of both the real and imaginary part of $\chi^{(2)}_{R}$ in "high resolution" using narrow line width picosecond pulses for both the IR and "visible" radiation.[26] Slightly later,[27,28] several groups employed broadband femtosecond IR radiation combined with narrow band picosecond "visible" radiation which in some cases is termed Heterodyne Vibrational Sum Frequency Generation, HD-VSFG, spectroscopy. In principle, both terms are applicable whether broadband or narrowband IR is utilised and are used interchangeably. In either technique, a reference beam, referred to as the Local Oscillator, LO, is generated, either from transmission of both the IR and "visible" beams through a noncentrosymmetric medium, such as ZnO,[29] or crystalline quartz,[26] or in reflection from a $KNbO_3$ surface.[27] Through transmission of the LO beam through transparent glass,[26,28,29] or by using a separate path and mechanical delay stage for the LO beam,[27] a time delay is introduced between the LO and the VSFG beam. When broadband IR radiation is used, following spectral dispersion, interference between the two beams results in a characteristic fringe pattern, referred to as a spectral interferogram, SI. A SI is produced using narrowband IR radiation by scanning the IR frequency; this technique provides robust stability over a wide IR frequency range, however, (at least) four scans of IR frequency is required to determine the absolute phase. The intensity detected in the HD-VSFG technique, $I_{\text{HD-VSFG}}$ is related to the electric field of the LO and VSFG, $\bar{E}_{\text{LO}}$ and $\bar{E}_{\text{VSFG}}$, respectively by:

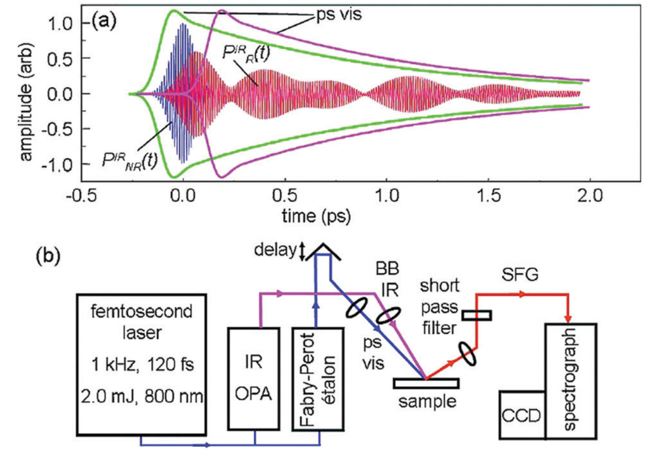

Fig. 3 (a) Suppression of SFG nonresonant (NR) background with a time-asymmetric visible pulse. A 100 fs IR pulse creates a polarization $P^{\text{IR}}(t) = P^{\text{IR}}_{\text{R}}(t) + P^{\text{IR}}_{\text{NR}}(t)$. The NR component, $P^{\text{IR}}_{\text{NR}}(t)$, has a faster time dependence, which tracks the IR pulse. The resonant part, $P^{\text{IR}}_{\text{R}}(t)$, due to molecular vibrational transitions, has a slower time dependence. SFG is created during the time that $P^{\text{IR}}(t)$ interacts with the time-asymmetric picosecond visible pulse. For clarity, optical-frequency oscillations in the visible pulses are not displayed. Two delay situations involving the time-asymmetric pulse are depicted. Either the visible pulse interacts with both $P^{\text{IR}}_{\text{R}}(t) + P^{\text{IR}}_{\text{NR}}(t)$ to generate resonant and NR signals or it is time-delayed beyond $P^{\text{IR}}_{\text{NR}}(t)$ to suppress the NR contribution, weakening the resonant contributions only slightly. (b) Block diagram of the laser apparatus. Part of the femtosecond pulse is used to generate a broadband infrared (BBIR) pulse in an optical parametric amplifier (OPA), and part is used to generate a time-asymmetric picosecond visible pulse in an etalon. Figure reproduced with permission from ref. 22.

$$I_{\text{HD-VSFG}} = |\bar{E}_{\text{LO}}|^2 + |\bar{E}_{\text{VSFG}}|^2 + \bar{E}_{\text{VSFG}}\bar{E}_{\text{LO}}\exp(i\omega t) + \bar{E}_{\text{VSFG}}\bar{E}_{\text{LO}}\exp(-i\omega t) \quad (6)$$

where t is the time delay between the LO and VSFG beams. The SI is inverse Fourier transformed in to the time domain; signal observed at $t = 0$ is due to $|\bar{E}_{\mathrm{LO}}|^2$ and $|\bar{E}_{\mathrm{VSFG}}|^2$, whereas signal observed at both positive and negative times, related to the time delay between the LO and VSFG beams, corresponding to the cross terms, $\bar{E}_{\mathrm{VSFG}}\bar{E}_{\mathrm{LO}}\exp(i\omega t)$ and $\bar{E}_{\mathrm{VSFG}}\bar{E}_{\mathrm{LO}}\exp(-i\omega t)$, respectively. Gating the signal at the positive time, and applying a Fourier transform back into the frequency domain, results in the real and imaginary parts of $\chi^{(2)}_{\mathrm{eff}}(\omega)$ being obtained. Referencing this signal against that obtained in the same manner for a sample without vibrational resonances allows the non-resonant signal to be removed, resulting in the real and imaginary parts of $\chi^{(2)}_{\mathrm{R}}$ to be obtained. The imaginary part of $\chi^{(2)}_{\mathrm{R}}$, $\mathrm{Im}\,\chi^{(2)}_{\mathrm{R}}$, is directly related to the vibrational resonances; deviation of $\mathrm{Im}\,\chi^{(2)}_{\mathrm{R}}$ away from 0 corresponds to a vibrational transition, with sign of the feature indicative of the dipole derivative vector, allowing information on molecular orientation to be inferred.[30] Further to this advantage, $I_{\mathrm{HD\text{-}SFG}}$ is proportional to the number density of surface species, rather than quadratically dependent as in the case for VSFG spectroscopy, significantly increasing the sensitivity of HD-VSFG, allowing vibrational resonances of adsorbed molecules with surface coverages as low as $\sim 3\%$ of a monolayer to be observed.[27]

Despite the obvious advantages of HD-VSFG spectroscopy, to the best of our knowledge no *in situ* electrochemical HD-VSFG has been published. This is a result of the challenging nature of the experiment, with dynamic measurements requiring long term stability of the relative phases of the LO and VSFG beams, along with the necessity for exact replacement of the sample with the reference sample to allow removal of $\chi^{(2)}_{\mathrm{NR}}$. It is our view that despite the challenges facing users of HD-VSFG spectroscopy, its advantages will result in reporting of systems under potential control in the near future.

A particular issue with the HD-VSFG techniques not mentioned thus far is the uncertainty in the measured phase due to the difficulty in placing the sample of interest and reference sample in the same position. Shultz *et al.* developed an alternative design for PS-VSFG using a non-linear interferometer with significantly improved phase-resolution, distinguishing it from other PS-VSFG techniques.[31,32] Narrowband infrared and visible pulses are split such that they are incident on a reference and the sample of interest simultaneously. The two sets of reflected SFG beams are then combined and interfere before detection. Further stability is provided by the use of an active feedback loop controlling the sample and reference positions using a tracker signal. More recently, the interferometer has been extended to use femtosecond IR lasers for broadband VSFG interferometry, speeding up acquisition times and providing similar levels of phase resolution to HD-VSFG.[33]

A natural extension of VSFG spectroscopy is to two-colour vibrational sum-frequency, 2C-VSFG, spectroscopy; here both the frequency of the IR and visible pulses are changed, and the resulting VSFG intensity plotted as a function of IR and visible frequency produces a 2C-VSFG spectrum. Yang *et al.*[34] employed a variation of the BB-SFG technique of Stephenson and coworkers,[20] in which broadband IR radiation is produced, along with tuneable, narrowband (<5 cm^{-1}) visible radiation, to monitor CO at a Pt(111) electrode under potential control. Along with changing vibrational character, the changing electronic structure could be monitored as a function of potential. Understanding the changing electronic structure of electrocatalysts during use is an important activity; however, in order to remove the complication of the observance of the non-resonant signal, it is our opinion that HD-VSFG experiments will need to be widely employed before 2C-VSFG will garner wider use for the study of electrode surfaces.

2 The study of heterogeneous electrocatalysis by VSFG

While VSFG spectroscopy was still in its infancy, three years after Shen and co-workers seminal report of the first SFG experiment,[18] Guyot-Sionnest and Tadjeddine applied VSFG to the prototypical system of CO adsorbed on a polycrystalline platinum electrode.[19] These spectra were shown to display potential dependent band positions, attributed to a well-known Stark effect,[35] which were in good agreement with those obtained in previous infra-red reflection absorption spectroscopy, IRRAS, studies.[36] Since this first electrochemical-VSFG experiment numerous experimental systems have been addressed. Initially these focused on small, prototypical species such as CO,[19] $\mathrm{CN^-}$,[37–45] and $\mathrm{SCN^-}$,[19] adsorbed on coinage metal electrode surfaces and later groups extended their works to examine the behaviour of wide range of larger molecules at electrodes under potentiostatic control ranging from small alcohols,[37–41,46–50] to complex aromatics[51–56] and ionic species[57,58] including ionic liquids.[59–62] Here in our discussion of heterogeneous electrocatalysis (Fig. 1(b), top) we focus on two particular classes of systems of relevance to the generation and utilisation of sustainable fuels. Initially we explore the behaviour of alcohols at electrode surfaces, experiments designed to improve our understanding of fuel cells. We then go on to examine the behaviour of water at charged interfaces, which can provide new insights into water electrolysers for hydrogen production.

2.1. Fuel cell chemistry

The oxidation of both methanol and ethanol are important processes in fuel cells. However, the oxidation of both alcohols results in the production of CO, which has a large affinity for common electrode materials (*e.g.* Pt) and, is an effective electrode poison making it important to understand the behaviour of bound CO under operating conditions.

Early VSFG studies on the oxidation of methanol in acidic solutions showed that multiple adsorption sites existed even on single crystal Pt electrodes. In addition to CO that was linearly bonded to a single Pt atom and bridge bonded CO to two Pt atoms, triply, or multiple, bonded sites which had not been previously detected by IR spectroscopy were observed.[40] Interestingly at low methanol concentrations CO occupied multi-bonded sites and only once the methanol concentration increased were linearly bound species observed.[40] At the most positive

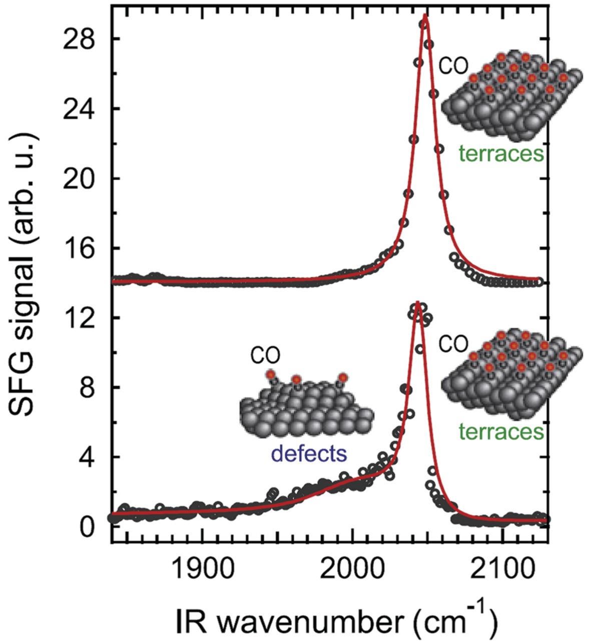

Fig. 4 Comparison of CO adsorption on Pt(110) electrode surfaces cooled in either Ar (top) or air (bottom), leading to the absence or presence of step defect sites, respectively. Electrodes were held at −0.1 V (*vs.* Ag/AgCl) in 0.1 M methanol in 0.1 M H_2SO_4. Reproduced with permission from Vidal *et al.*[48]

potentials studied (where oxidation of CO to CO_2 is efficient) the VSFG signals of adsorbed CO were negligible.[40]

The frequency of the C–O stretch is also particularly sensitive to the local density of CO groups as strong dipolar coupling between adsorbed CO molecules also result in a shift in vibrational wavenumber, allowing a relative concentration of adsorbed CO molecules to be determined. This has been exploited by Vidal *et al.*, who studied the concentration, potential and electrode preparation dependence on the methanol dissociative adsorption on a Pt(110) electrode, Fig. 4.[48] Concentrations of methanol of ∼0.1 mol L^{-1} resulted in a shift in the CO vibrational wavenumber on the terrace sites, indicative of dense packing. As the potential is made more positive the efficiency of CO oxidation increased and the VSFG signal of the terrace sites was observed to decrease sharply, in-line with previous works.[40] Intriguingly the intensity of bands corresponding to CO bound to step sites (defects), remained constant across the potential range studied despite both sites being readily populated by CO at less positive potentials.[48] This led to the suggestion that CO oxidation to CO_2 occurred at the less-densely-populated step sites, in which co-adsorption of O_2 can occur. Following CO_2 desorption CO diffusion from terrace sites to the vacant step sites occurred, maintaining $CO_{(ad)}$ concentration at step sites and decreasing terrace site number density.[48]

Although derivation of the changing relative surface concentration of a species during an electrochemical experiment is feasible it is important to recognise the complexity of the factors determining the frequency of the VSFG bands. In addition to being sensitive to the relative surface concentration, site and geometry of adsorption the C–O stretching frequency will also be dependent upon the external field arising from the bias applied to the electrode.[63–65] Therefore disentangling individual contribution is complex. In systems where it is known that no changes in binding orientation occurs with changing coverage or applied potential simplified two component models to separate surface coverage and external field effects, such as the one recently described by Pfisterer *et al.* for the analysis of SEIRAS data,[64] and applied by us for VSFG,[25] can be used.

The mechanisms of electrochemical oxidation of ethanol are more complicated than that of methanol, with VSFG spectroscopy playing a key role in unravelling this mechanism. Works on the topic prior to 2013 are extensively reviewed elsewhere[66] and are only mentioned briefly here. Although the majority of early studies focused on the production of adsorbed CO[67–69] a breakthrough was the observation of the potential dependence of many key intermediate species by Kutz *et al.*[70] who, employed VSFG spectroscopy to derive a mechanism for the oxidation of ethanol upon which Fig. 5 is based. Overall, ethanol may be oxidised by dehydrogenation to acetaldehyde in solution, which along with ethanol, is adsorbed to the electrode surface. Here, both species rapidly decompose into CH_x and CH_xO species, which undergo oxidation to CO, which undergoes further oxidation to CO_2. CO may be produced by oxidation of either CH_x or CH_2O; in order to investigate this further the dissociative adsorption and subsequent electrochemical oxidation of isotopically labelled $^{12}CH_3{}^{13}CH_2OH$ was monitored using VSFG spectroscopy. A significantly larger VSFG signal was observed for ^{13}CO than ^{12}CO, indicative that the oxidation of CH_xO is facile compared to that of CH_x.[70]

Particularly pertinent for efficient ethanol oxidation is the possibility that adsorbed acetaldehyde may oxidise to form acetate, which may only desorb when converted to acetic acid, which in principle can be oxidised to CO_2, but not at fuel cell relevant potentials.[70] The acetate anion has been observed with VSFG spectroscopy, which intriguingly, is present in a larger potential window, and a greater number density, in sulphuric acid solutions than perchlorate acid solutions, Fig. 6. Vibrational resonances assignable to (bi)sulphate species are observed along with those of the acetate anion; co-adsorption of (bi)sulphate is thought to not only stabilise the adsorption of acetate anions, but also confines them in a more ordered structure.[70] These findings have consequences for the use of dilute sulphuric acid in fuel cells: the stabilisation of acetate species on the electrode surface by (bi)sulphate species blocks catalytic sites lowering activity. Gomes *et al.*[71] observed many

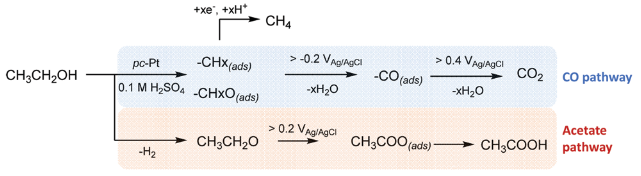

Fig. 5 Proposed mechanisms of ethanol oxidation at polycrystalline (pc) Pt in 0.1 M H_2SO_4 based on VSFG analysis, figure based on ref. 70.

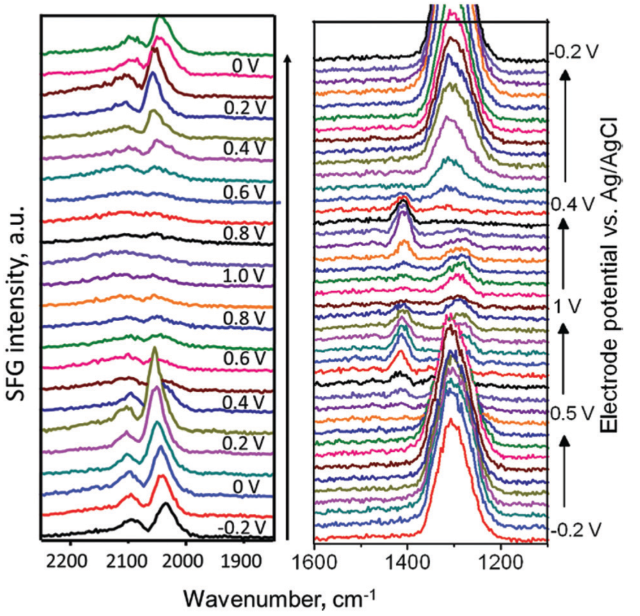

Fig. 6 Potential-dependent VSFG spectra of (a) 0.2 M $^{13}CH_3{}^{13}CH_2OH$ in 0.1 M $HClO_4$ and (b) 0.5 M $^{12}CH_3{}^{12}CH_2OH$ in 0.1 M H_2SO_4, including resonant contributions from acetate and bi(sulfate) as well as NR background, reproduced with permission from ref. 70.

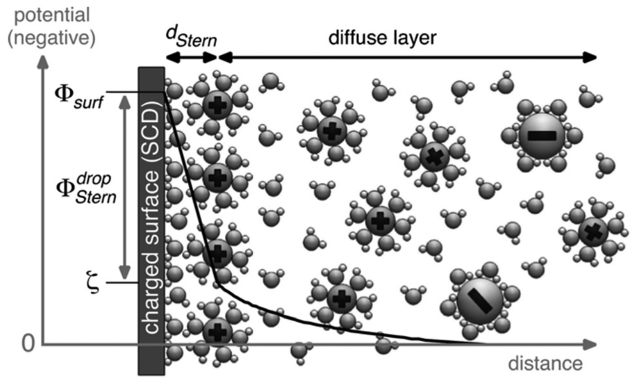

Fig. 7 Gouy–Chapman–Stern model of the aqueous electrode/electrolyte interface, with a negative surface charge density (SCD) and ordering of cations close to electrode surface, overlaid with the corresponding potential profile. Reproduced with permission from ref. 73.

more adsorbed species on a polycrystalline platinum electrode, including the reactive methoxy and ethoxy species; notably, at potentials above 0.9 V an increase in adsorbed oxide species was observed, which block catalytic sites, preventing adsorption of further ethanol molecules, effectively inhibiting C–C bond cleavage.[71] Very recently, Dewan *et al.*[72] compared the role of C–C bond breaking and ease of oxidation of CH_x and CH_xO fragments by following the oxidation of ethanol and ethylene glycol on polycrystalline platinum electrodes using VSFG. Ethylene glycol was shown to undergo more efficient C–C cleavage and complete oxidation, concluded to be facilitated by the presence of a second hydroxyl group, in line with the earlier findings of Kutz *et al.*[70]

2.2. Water at electrode interfaces

The direct electrocatalytic splitting of water to hydrogen and oxygen is another key process in the development of sustainable fuels. Electrochemically, this process can be split into two half reactions involving either hydrogen evolution (HER) or oxygen evolution (OER). Developing efficient OER & HER catalysts can be accelerated with an improved understanding of the underlying catalytic mechanisms. A detailed understanding of the electrode/water interface, which is common to both the OER & HER, could therefore aid the understanding of catalytic processes occurring at both types of aqueous interface.

In situ electrochemical experiments on such catalytic surfaces would necessarily involve recording VSFG spectra of charged surfaces, introducing additional complications from third order (χ^3) contributions.[17] An understanding of the Gouy–Chapman–Stern electrochemical double layer (EDL), shown in Fig. 7,[73] can help understand this. Supporting electrolyte salts in the aqueous solution form a compact layer of counter ions close to the surface to oppose the surface charge and a more diffuse layer of ions extend further into the solution. The distance this diffuse layer penetrates into the bulk, the Debye length (λ_D), is determined by the strength of the surface electric field. The 3rd order susceptibility arises from the ordering associated with this electric field, allowing molecules within both the compact (Stern) and diffuse layers to contribute to the observed VSFG signal. As a result, at least three distinct types of water structure can be expected, including a bound interfacial layer (BIL), quasi-ordered water in the EDL and SFG-transparent bulk water.[74] The size of the EDL, and consequently the distance away from the surface that molecules can still contribute to the SFG signal, can be influenced by the concentration of the supporting electrolyte. Increasing this salt concentration forms a more compact layer of counter ions near the interface, screening the surface charge and shrinking λ_D. This phenomenon has been experimentally exploited by several groups and allows a mechanism for separating the second and third order contributions to gain a better understanding of the interface under study.[75–80] Interestingly, the identity of the cation also has a significant impact on the effective screening of surface charge, with multivalent cations, such as Ca^{2+} and Mg^{2+}, more efficiently suppressing the surface electric field.[81]

VSFG has been extensively used to study the water structure at charged surfaces, such as SiO_2,[82] Al_2O_3,[83,84] and even CaF_2,[85,86] with a focus on the O–H stretch spectral region. In these cases, the interfacial electric field arises from charging of the surface, which can be manipulated through control of the bulk pH, *i.e.* protonation or deprotonation. Typically 2 broad resonant features are seen at around 3200 & 3450 cm^{-1}, as shown in Fig. 8 for the silica/water system.[87] These were initially assigned to an ice-like symmetric OH stretch at 3200 cm^{-1}, indicative of an ordered H-bonding environment and an OH stretch for more disordered H-bonded water at 3450 cm^{-1} (labelled liquid-like) by Shen *et al.*[88] A weak shoulder was also observed $\sim$3600 cm^{-1}, assigned to the forbidden antisymmetric O–H stretch of asymmetrically bound water, though a similar feature at 3650 cm^{-1} has since been attributed to the O–H stretch of weakly H-bonded water.[89,90]

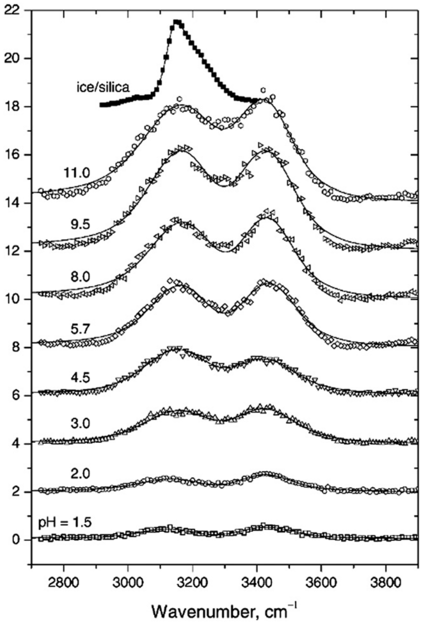

Fig. 8 VSFG spectra of water/α-quartz (0001) interface at various bulk pH values (as well as ice/silica for comparison) in SSP polarisation of SFG, "visible" and IR respectively. Reproduced with permission from ref. 87.

In the original study a 180° change in the phase of the SFG signal was observed when the bulk pH was varied from 1.5 to 12.3, where the silanol surface groups are expected to be either fully protonated or deprotonated, respectively.[88] This phase change provided the first direct spectroscopic evidence for water molecules flipping their orientation near the surface to have hydrogen pointing away from the surface when it is positively charged or at the surface when it is deprotonated. Additional PS-VSFG experiments by Shen *et al.* have since further deconvoluted the ice-like peak into two; a negative feature centred around 3000 cm^{-1} and a positive feature at 3200 cm^{-1}, corresponding to the opposite orientations of water following the aforementioned pH-dependence.[91]

The assignment to two distinct hydrogen bonding environments has since been disputed by Sovago *et al.*,[92] who argue that the double-peak structure in homodyne (non-phase-sensitive) VSFG spectra arises from coupling of the symmetric OH stretch by a Fermi resonance with the overtone of the H–O–H bending vibration; with the transition from the zero-point vibrational level to the latter, forbidden in the IR and Raman spectrum within the harmonic approximation. They show that this intramolecular vibrational coupling can be suppressed through gradual isotopic dilution of D_2O with H_2O, producing differing relative concentrations of HOD molecules, resulting in a smooth transition from two peaks to one being observed in the VSFG spectrum. In the mixed HOD species, neither the independent O–H nor O–D stretches occur at vibrational wavenumbers which are accidentally degenerate with that of the overtone of the H–O–D bend, resulting in the non-observance of this vibration in the VSFG spectrum of the isotopically diluted system. The technique of isotopic dilution has previously been shown to distinguish separate vibrational structures at the air/water interface.[93] More recent studies by Tahara's group, using a similar isotopic dilution experiment but with phase-sensitive HD-VSFG, have provided further evidence that intramolecular vibrational coupling is the cause of the doublet peak structure in the O–H stretch region.[94–96] Phase information gained from these studies also provides additional information on the net orientation of water at the silica interface. At basic pH values, a single positive feature is observed corresponding to a net H-up (hydrogen atoms pointing at the surface) water orientation. As the bulk pH is changed to neutral, two features with opposite phase appear, indicating that both the H-up and H-down orientations of water are present as the surface charge transitions from fully deprotonated towards a fully protonated surface. As an aside, the use of D_2O for these experiments presents an additional advantage for homodyne VSFG experiments, as the vibrational lifetime of the O–D stretch (∼2 ps) is significantly longer compared to the O–H stretch (∼1 ps).[97] Since the main method of non-resonant suppression in homodyne SFG is to introduce a time delay between the visible and IR pulses, the longer lifetime of the O–D vibration provides a wider temporal window for such experiments.

As discussed above, the concentration of the supporting electrolyte can suppress the electric field extending from the surface.[98] The SFG signal for water in the BIL should be independent of this salt concentration, thus any constant SFG signal as the electrolyte concentration is varied can be attributed to water in the BIL, while the variable part of the signal is associated with water further away in the EDL. Urashima and co-workers applied this technique to experimentally extract the structure of the BIL in the silica/water system with a fully deprotonated surface (at pH 12) using HD-VSFG.[94] A positive feature, corresponding to water with H pointing at the surface silanolate groups, remains when subtracting away the diffuse layer contribution to the spectrum. Wen *et al.* and Pezzotti *et al.* have also provided computational frameworks for separating the BIL response from the diffuse layer response at charged aqueous interfaces.[74,99] These methods of deconvolution should be universally applicable as the water structure induced by a given electric field will be largely independent of the nature of the surface under study; structural differences across materials should only impact water structure in the BIL, making this a potentially powerful tool in understanding potentiostatically controlled systems, where the surface electric field is more rigorously controlled.

The doublet structure in the O–H stretching region has been studied in detail in the references above, however, other water vibrational modes have also been investigated and could provide additional or complimentary information. For example, the air/water interface includes a peak around 3700 cm^{-1} for the vibrations of free (non H-bonded) O–H groups,[93,100] with a similar feature often observed for surface hydroxyl groups on hydrophobic oxide surfaces.[84,90,101] The presence or absence of this peak provides information on the hydrophobicity of the surface and can therefore be correlated to changes in the surface structure, including charging of surface hydroxyl moieties.

The water bending vibrations at the silica/water interface have not been directly probed. However, the comparatively much weaker [stretch + bend] combination band between 5000 and 5300 cm^{-1} has been explored.[102] The most intense band in this region is observed at 5200 cm^{-1}, which is blue-shifted around 100 cm^{-1} from the analogous peak in the FTIR and Raman spectra. It is unclear in this case whether the significant blue-shift in the combination band is primarily from the blue-shift of the bend frequency or combination with the weakly H-bonded O–H stretch of stretch at 3650 cm^{-1} instead of the more strongly H-bonded stretches around 3400 cm^{-1}. Previous studies have noted a smaller blue-shift ($\sim$20 cm^{-1}) of the bend vibration at the air/water interface compared to bulk water,[103,104] supplementing the red-shift observed in the O–H stretch region as an indication of increased H-bonding and ordering, though this likely doesn't fully account for the observed blue-shift. Despite the smaller transition cross-section and ambiguity in assigning the exact components of the combination band, which can be clarified with a better understanding of the O–H stretch contribution, this indirect method of detecting the bend vibration is an elegant means of accessing spectral regions which were previously unattainable due to attenuation of IR light by the substrate itself.

At the air/water interface, the low wavenumber librational motion of water has also been studied. A vibrational mode was observed at 834 cm^{-1}, more than 100 cm^{-1} higher than that of bulk water, again providing evidence of a more ordered (ice-like) structure of water at an interface.[105] Tong *et al.* have also explored this spectral region to investigate the dissociative adsorption of water on a well-defined α-alumina(0001) surface.[106] The introduction of water on the UHV-prepared surface was monitored by the response of the Al–O phonon modes below 1000 cm^{-1}, as well as in the O–H stretch region. The growth of Al–O–H bend vibrational modes between 850 and 950 cm^{-1} is concurrent with the appearance of a non-H-bonded Al–O–H stretch around 3700 cm^{-1}. However, the quantitative surface coverage information gained from the two spectral regions is not consistent, with the stretch region indicating a 90% level of hydroxylation and the bend region suggesting only 60% hydroxylation. This highlights the difficulty in using a nonlinear spectroscopy to gain quantitative surface coverage information, though this has recently been addressed by Koehler *et al.* who were able to directly gain surface coverages of functionalised graphene.[107]

Water structure at semiconductor surfaces represents the next step towards understanding the OER and HER mechanisms on the Earth-abundant oxide electrocatalysts that are currently being researched intensely by materials development groups. Kataoka *et al.* showed that the water structure at the surface of TiO_2, a promising semiconductor material for water splitting, shows a similar doublet structure in the O–H stretch region that can be disrupted by the binding of phosphate ions.[108] In this study a TiO_2 layer is deposited on a SiO_2 substrate and the incident IR and "visible" fields pass through the silica before reaching the TiO_2 water interface. Moving towards studying such multi-layered materials requires careful accounting for changing Fresnel reflections as a function of IR wavelength to correctly interpret broad resonant signals. Backus *et al.* provide an excellent framework for accomplishing this and apply it to the study of the TiO_2/water interface, where PS-VSFG is used to distinguish the orientation of chemisorbed and physisorbed water.[15,109] An interesting aspect of TiO_2 is that surface hydrophilicity can be increased upon UV illumination. This was monitored spectroscopically by Uosaki *et al.*, who observed an increase in the O–H stretch bands as result of an increase in adsorbed water concentration and ordering of water at the surface after UV pre-treatment.[110]

The VSFG experiments discussed thus far have involved infrared-transparent mineral surfaces, allowing the incident IR and Vis fields to reach the interface through the mineral itself. In order to progress to studying active electrode materials, which typically contain an IR-opaque conductive layer, an alternative experimental geometry is required involving the IR and "visible" fields reaching the interface through the electrolyte. While *in situ* electrochemical VSFG experiments in organic solvents have been explored for a variety of systems,[17] the analogous aqueous experiments prove to be experimentally more challenging due to the significant attenuation of IR light across most of the MIR spectral region, as shown in Fig. 9 (using molar absorption coefficient data from Bertie *et al.*)[111] As such, very few investigations have been carried out on the electrode/water interface under potentiostatic control. Uosaki *et al.* first looked at the interfacial water structure for systems under potentiostatic control on both gold and platinum electrodes.[112–114] As with applying the charge by bulk pH control, the potential-dependent VSFG spectra can be understood by reorientation of water in line with the charging of the surface, with a minimum in VSFG intensity around the point of zero charge (PZC) for the materials. Similarly, Gewirth *et al.* have studied the potential-dependent water structure at silver electrodes, again observing various types of water structures at the surface and in the EDL that show a minimum in intensity around the PZC. To avoid gas bubble evolution interfering with

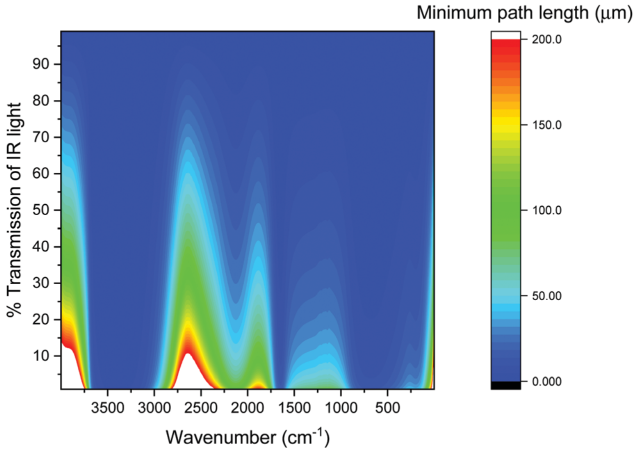

Fig. 9 Minimum path length required to get appreciable transmission of IR light, where blue areas represent significant attenuation of IR light. Calculated using molar absorption coefficient data from Bertie *et al.*[111]

spectroscopic measurements, these studies did not probe potentials at which the OER and HER reaction occur. The experimental cell setup developed by Verreault *et al.* overcomes some of the practical obstacles associated with these experiments by probing through a very thin (∼100 nm), IR-transparent, conductive indium tin oxide (ITO) layer, allowing *in situ* electrochemical VSFG spectra of the ITO/water interface in the O–H stretching region between −2 and +2 V (*vs.* Ag/AgCl) to be obtained.[115] The potential-dependent spectra also show the double-peak structure with a minimum around the PZC for the ITO surface, although the potential regime studied may also introduce complications from reduction (and subsequent partial re-oxidation) of indium and tin during potential cycling.[116] *In situ* electrochemical studies using a thin electrolyte layer are not ideal for all systems, especially when reaction kinetics are limited by mass transport of species between the electrode surface and bulk electrolyte. As such, future work using similar IR-transparent conductive layers and probing through the electrode instead of the electrolyte could solve the problem of gas evolution, attenuation of IR light, as well as allowing the use of larger electrolyte volumes, enabling *in situ* VSFG studies of the OER and HER under more realistic condition.

VSFG spectroscopy has already been employed in order to study hydrogen adsorption on Pt surfaces,[38,45,117,118] an important step in the hydrogen evolution reaction. Potential-dependent vibrational resonances are observed for various types of adsorbed hydrogen species between 1800 and 2020 cm^{-1}, as well as a potential dihydride HER intermediate at 1770 cm^{-1}. The frequencies of these vibrations are also shown to depend on the nature of water structuring in the EDL, leading to different levels of H-bonding, highlighting the need to understand structuring of water both at the surface and in the EDL.

These initial VSFG studies of potential-dependent water structure at electrode surfaces open the door to an exciting new direction for experiments investigating both the OER and HER. Not only can the electrocatalytically active water be studied, but control of electrolyte salt concentration can aid in separating the 2nd and 3rd order contributions potentially allowing water in EDL and BIL to be discriminated. There is also precedence for *in situ*-VSFG of photocatalytic experiments under illumination,[119] which could facilitate the study of photocatalysts and photoelectrodes under operating conditions. Furthermore, the continued improvement in optical parametric amplifiers capable of providing significant laser intensities at low (<1200 cm^{-1}) wavenumbers, such as those used to study the librational motion of water,[105] provide access to a previously unexploited spectral region. This lower wavenumber region is particularly attractive as the O–O bond forming intermediates on various electrocatalysts for water splitting, including nickel oxyhydroxide,[120] cobalt oxide,[121] hematite,[122,123] strontium titanate[124,125] and iridium oxide,[126–128] have been shown to have vibrational modes between 700 and 1200 cm^{-1} using a range of surface-sensitive IR and Raman spectroscopies. Despite several years of investigation, the proposed mechanisms for each of these electrocatalysts include many more as-yet-undetected catalytic intermediates. Applying the surface-specificity and extreme sensitivity of VSFG to these systems could help detect low surface concentrations of key intermediates, enabling a more detailed mechanistic understanding that can help drive improved materials design.

3 VSFG of molecular electrocatalysts

Molecular electrocatalysts, which are typically small molecules with well-defined structures which are initially oxidised or reduced at the electrode surface (Fig. 1(b), middle/bottom),[129] are being intensively studied for a wide range of transformations related to sustainable fuel generation and utilisation including; O_2 reduction, H_2 evolution, H_2O oxidation and CO_2 reduction.[130] Interest arises both from the possibility to design catalysts that utilise high abundance, lower cost, elements and through the possibility to deliver improved selectivity's and activities by control of the catalysts ligand architectures. Given the high degree of synthetic control achievable a particularly acute need exists for mechanistic details to enable the rational design of the catalyst structure.[131]

3.1. Covalently immobilised (heterogenized) catalysts

Once active molecular electrocatalysts are developed they are often heterogenized through attachment to an electrode support to facilitate catalyst recovery/separation during application. This binding of the catalyst has additional benefits for VSFG spectroscopy as it provides materials with ordered catalyst layers, enhancing the intensity of detected signals. Therefore, to date the majority of the VSFG studies of molecular electrocatalysts for energy applications have focused on the orientation of the catalyst at the surface,[132–139] which can have a profound impact on the observed activity. Early works by the Lian group used VSFG spectroscopy to study a series of Re bipyridine carbonyl complexes, which are known to be active as both CO_2 reduction electrocatalysts and photocatalysts, immobilised on TiO_2.[132,133] In all systems studied the presence of carboxylate groups to the bipyridine ligands ($[Re(L_nC)(CO)_3Cl]$, where L_nC = 2,2′-bipyridine-4,4′-$(CH_2)_n$-COOH, n = 0–4), enabled covalent immobilisation on TiO_2 with the bipyridine group approximately perpendicular to the surface exposing the catalytic site (Fig. 10). Interestingly both VSFG and PS-VSFG showed that the tilt angle of the catalyst on TiO_2 is strongly dependent upon both the length of the methylene linker of the anchor group and the nature of the TiO_2 surface.[133] Clear differences in binding geometry and vibrational dynamics have also been reported by several groups between (001) and (110) surfaces[134,138] giving rise to the structural heterogeneity of the catalyst when bound to nanocrystralline TiO_2 surfaces, as identified by 2D-VSFG measurements.[139]

Although these measurements clearly show the potential for VSFG to probe a molecular catalyst for CO_2 reduction at an electrode surface,[140] they were performed in the absence of electrolyte and without the application of an applied bias limiting the level of insight that can be drawn. The lack of *in situ* potential dependent VSFG spectroscopy is likely in part due to the challenging

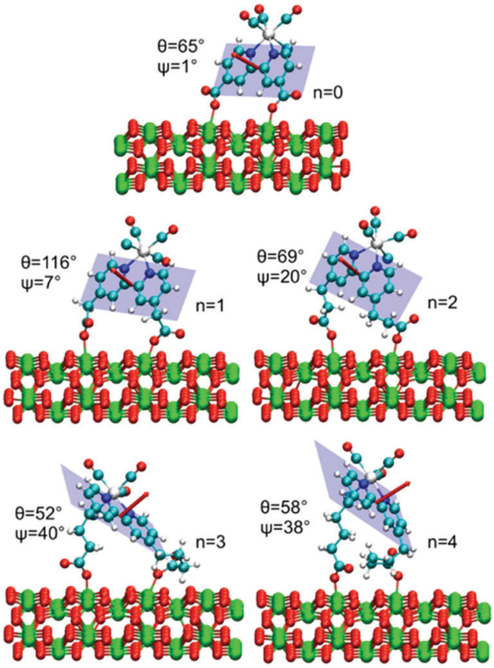

Fig. 10 Optimized binding structures for ([Re(L$_n$C)(CO)$_3$Cl]) on rutile TiO_2(001) as the linker length is modified. The calculated structures show good agreement with the average orientation angles found experimentally by phase-sensitive VSFG spectroscopy. Figure reproduced with permission from ref. 133.

potential-dependent optical behaviour of TiO_2 electrodes in the visible to nIR region.[141] Therefore, there is particular interest in developing complexes which can be immobilised on more traditional electrode materials and a series of papers have studied [Re(4,4′-dicyano-2,2′-bipyridine)$(CO)_3$Cl] at Au surfaces.[136,137] Initially, VSFG and HD-2DVSFG of the catalyst in the absence of electrolyte were carried out, providing the ensemble averaged surface orientation of the complex where the catalytic centre found to point away from the surface and with the plane of the bipyridine ligand is tilted ($\sim 60^\circ$) with respect to the surface. Although the catalyst was shown to be electrochemically active in solution catalysis itself was partially deactivated by the cyano groups and the weak binding of the complex to gold also further hindered *in situ* spectroscopic studies during catalysis.[136] In 2018 to overcome these limitations rhenium and manganese analogues were prepared with thiol groups present allowing for the formation of a self-assembled monoloayer of the catalyst on an electrode enabling *in situ* VSFG studies.[142] Here the authors were able to measure the Stark tuning of the ν(CO) modes of the catalyst on the electrode surface prior to reduction. Utilising this VSFG data and DFT modelling it was possible to evaluate the local electric field strength for each catalyst at the surface, highlighting that catalysts experience very large electric fields (10^8–10^9 V m^{-1}). Although the potential window of operation was limited by reductive thiol desorption preventing any reductions at the catalyst from being measured, this first study of a covalently immobilised CO_2 reduction catalyst under potential control using VSFG spectroscopy represents an important milestone for the field. It highlights the capability of the technique to gather detailed information not just on the geometry of the catalytic centre itself but also to report on the large electric fields which are likely to be critical in controlling activity.[142]

3.2. Solution electrocatalysts for CO_2 reduction

Despite heterogenization often (but not always) being the ultimate goal of the catalyst development programme, the vast majority of molecular electrocatalytic studies are carried out with the catalyst in solution. The ease of electrochemical evaluation enables researchers to rapidly examine the behaviour of synthetic modifications, prior to immobilisation. However, such an approach makes mechanistic studies challenging. Intermediate species, which control the observed activity are likely to only be short-lived following electron-transfer from the electrode to the catalytic centre making their detection challenging. Many traditional spectroelectrochemical methods require the build-up of a significant concentration of the species of interest in the bulk to enable detection.[131] Therefore, surface-specific VSFG spectroscopy is a potentially powerful tool for mechanistic studies which can report on the roles of electrode–catalyst interactions and electric field in determining reaction pathways.

In contrast to hetereogenized molecular electrocatalysts where permanent ordering at the electrode surface occurs, the study of solution electrocatalysts relies on the formation of transiently ordered layers of catalysts at, or on the electrode surface to enable the detection of a significant VSFG response. At its most extreme, the ordered catalyst layer can be in the form of an absorbed layer and as early as the 1960's it was recognised by Anson and co-workers that metal complexes in solution could reductively adsorb onto electrode surfaces.[143] Since then the potential dependent formation of ordered adsorbate layers has since been widely studied using VSFG spectroscopy to address systems as diverse as solvent structures at Li-ion battery electrodes[144,145] to the orientation of biomolecules at a glassy carbon electrode.[55] It is also well understood that ordering of the electrolyte and analyte can occur within the double layer structure due to electric field induced dipole alignment. Indeed, the detection of non-specifically adsorbed species in the presence of an electric field by VSFG spectroscopy is well-established and discussed above in Section 2.2. that explores the application of VSFG to study water close to electrode surfaces in the presence of an electric field.[58,75,88,94] Despite this literature precedence, we were surprised to note that when we began to carry out VSFG studies of electrochemical interfaces around 2015 that, to the best of our knowledge, the mechanisms of molecular electrocatalysts in solution had not been previously studied by VSFG spectroscopy. Numerous ''solution'' CO_2 reduction electrocatalysts[146–149] are known to show a strong dependence on the nature of the electrode material used indicating that transient adsorption is occurring and that electrode–catalyst interactions can influence the mechanisms, making them ideal systems for VSFG spectroscopy. Therefore, our early experiments focussed on one such class of CO_2 catalysts, [M(bpy)$(CO)_4$] (M = Mo, W, Cr), which have been studied by both the groups of Kubiak[150] and Hartl.[147] Despite the utilisation of both Mo and W in biological systems for CO_2 interconversions remarkably few synthetic group 6 catalysts for CO_2 reduction are known. Therefore even though early reports indicated disappointing activity $[M(bpy)(CO)_4]$ when compared to analogous group 7 metal carbonyl complexes, interest in these catalysts continues to grow.[151–153] One of the most striking features of the work of Hartl *et al.*,[147] was the strong dependence of the onset of catalysis on the nature of the electrode material and the solvent utilised. On Au electrodes the onset for catalysis shifts +0.6 V, compared to on Pt and glassy carbon. On the basis of electrochemical and bulk spectroelectrochemical measurements the scheme on the right of Fig. 11 was proposed.[147] Briefly, initial reduction gives rise to $[M(bpy)(CO)_4]^{\bullet -}$ which then undergoes a 2nd reduction on Pt to form $M(bpy)(CO)_4{}^{2-}$ which fragments to form $[M(bpy)(CO)_3]^{2-}$, the active catalyst that can then bind to CO_2. On Au it was hypothesised that the initially formed $[M(bpy)(CO)_4]^{\bullet -}$ was able to directly fragment on the electrode surface to yield $[M(bpy)(CO)_3]^{\bullet -}$ which could then be reduced to form the active catalyst at a more positive potential. Using VSFG we examined the electrochemistry of $[Mo(bpy)(CO)_4]$ at both Au and Pt electrodes in the presence and absence of CO_2 to explore the nature of the electrode–catalyst interactions under potentiostatic control, Fig. 11.[154] Measurements of Au electrodes during cyclic voltammograms, even at scan rates of up to 50 mV s^{-1} with spectra recorded every 1 s, clearly showed VSFG bands assignable to the ν(CO) modes of the different electrochemically generated species at, or close to the electrode surface. Notably in contrast to bulk spectroelectrochemical methods the intrinsic interface selectivity of VSFG enabled detection of $[Mo(bpy)(CO)_3]^{2-}$ at the Au electrode surface at potentials approximately 0.5 V positive of the reduction potential of $[Mo(bpy)(CO)_4]^{\bullet -}$ confirming the previously hypothesised mechanism. Perhaps counter-intuitively on Pt, a metal which forms stronger M–CO bonds, CO loss from $[Mo(bpy)(CO)_4]^{\bullet -}$ was not detected. This behaviour could be rationalised through analysis of the potential dependence of the non-resonant response (as an indicator of local electric field), the intensity of the VSFG bands assignable to the acetonitrile solvent and the observed electrochemically generated species. Upon reduction of $[Mo(bpy)(CO)_4]$ a large reorganisation of the surface species occurred and $[Mo(bpy)(CO)_4]^{\bullet -}$ appears to be able to displace solvent and electrolyte from the Au surface, enabling fragmentation. In contrast $[Mo(bpy)(CO)_4]^{\bullet -}$ showed minimal interaction with the Pt surface a finding supported by analysis of the apparent Stark tuning rate indicated and the noted lower intensity of the VSFG ν(CO) bands of the complex indicating a lesser degree of ordering of the interface.[154]

More recently we have studied the related group 7 complex $[Mn(bpy)(CO)_3X]^{n+}$ (where $X = Br^-$ ($n = 0$) or solvent ($n = 1$)) using VSFG spectroscopy. This class of Mn complexes are very widely studied molecules for electrocatalytic CO_2 reduction[155–157] due to them being composed of abundant elements, their low onset potential and their high selectivity towards CO production. However, many mechanistic details remained unproven and experimental verification of proposed, likely short-lived, catalytic intermediates had not been possible for several key species.[157–159] Early on we found that the electrocatalytic currents achievable with $[Mn(bpy)(CO)_3X]^{n+}$ is largely insensitive to the choice of electrode material, allowing us to employ Hg/Au amalgam electrodes for VSFG experiments.[25] This is important as the Hg/Au amalgam

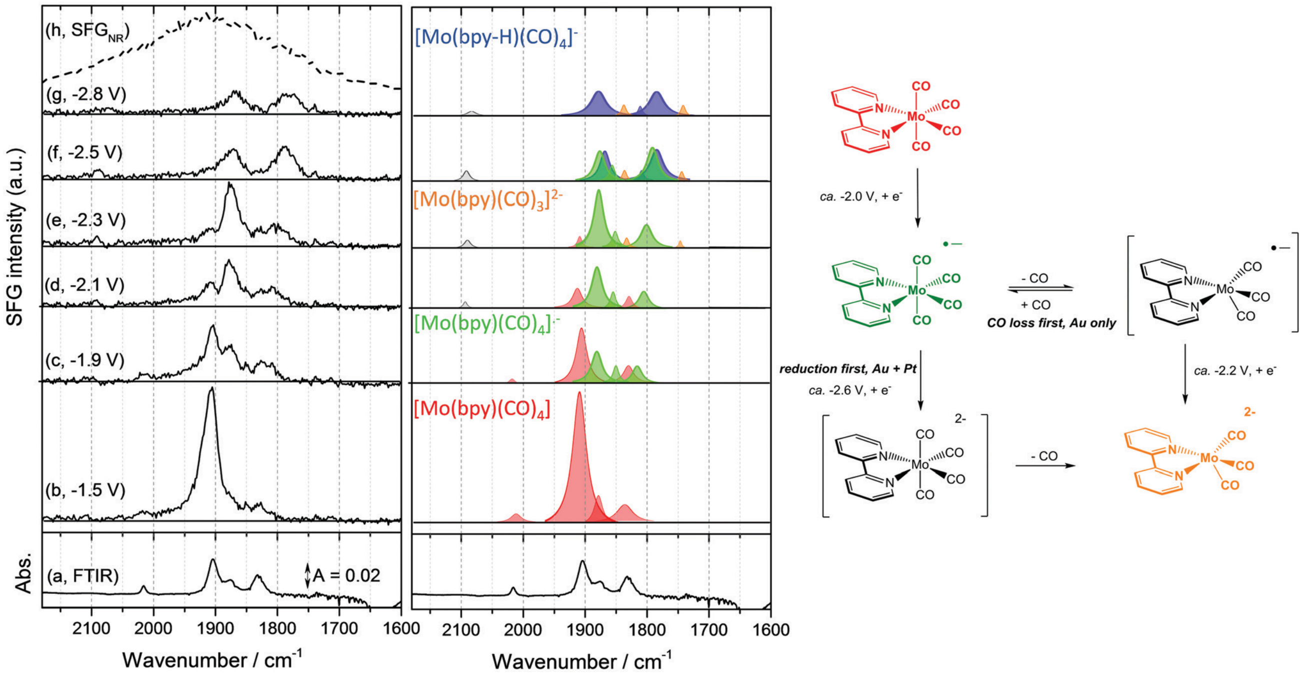

Fig. 11 Left: Solution phase FTIR (a) and *in situ* VSFG spectra (b–g) of $[Mo(bpy)(CO)_4]$ (1 mM) at a Au electrode in CH_3CN and 0.1 M $TBAPF_6$ under Ar. Centre: Pictorial representation derived from multi-Lorentzian fits of the experimental data showing the dominant species at the electrode surface. Right: VSFG experiments confirmed the electrochemical pathways of $Mo(bpy)(CO)_4$, Figure reproduced with permission from ref. 154.

provides a suitably reflective surface for VSFG and critically a surface that has a low affinity for CO. In addition to helping prevent catalyst fragmentation the low CO affinity was also found to be beneficial as it prevented electrode fouling by CO. Our earlier studies of Mo(bpy)(CO)$_4$ in acetonitrile allowed us to generated a detailed understanding of the mechanism of formation of the catalytically active species ([Mo(bpy)(CO)$_3$]$^{2-}$) from the starting material. However, individual species within the catalytic cycle could not be detected by VSFG spectroscopy. Instead, the build up of Au–CO under catalytic conditions dominated the spectra recorded.

VSFG experiments using the Au–Hg electrodes indicated that the mechanism of formation of the dominant electrocatalytically active species, [Mn(bpy)(CO)$_3$]$^-$, occurred by the same route as previously observed using other electrode materials. There [Mn(bpy)(CO)$_3$X]$^{n+}$ undergoing a one electron reduction and subsequent dimerization to form [Mn$_2$(bpy)$_2$(CO)$_6$] which can then be reduced to form [Mn(bpy)(CO)$_3$]$^-$.[24,160] Interestingly, [Mn(bpy)(CO)$_3$]$^-$ could not be directly observed by VSFG spectroscopy, despite it being stable during bulk electrolysis FITR experiments. Instead VSFG spectra showed that the presence of even trace levels of protons from the electrolyte lead to rapid formation of [Mn(bpy)(CO)$_3$H], a precursor to H$_2$ production. In the presence of CO$_2$ and a suitable acid source [Mn(bpy)(CO)$_3$H] is not formed and instead several new VSFG bands are observed at potentials beyond the onset for catalysis, Fig. 12.[24] Through a combination of experiments using a range of different acids, isotopically labelled CO$_2$ and theoretical modelling of the vibrational modes in the presence of the changing electric field the bands were assigned to [Mn(bpy)(CO)$_4$]$^+$ a species on a previously hypothesised catalytic pathway, labelled "protonation first", due to the nature of the initial step and the need for a strong acid source.[24] We have also used VSFG spectroscopy to study the behaviour of [Mn$_2$(bpy)$_2$(CO)$_6$] at the electrode surface and also shown that [Mn$_2$(bpy)$_2$(CO)$_6$] directly interacts with the CO$_2$ and H$^+$ to initiate catalysis *via* a low overpotential pathway.[25] Direct observation of catalytic intermediates of this pathway by VSFG spectroscopy was not achieved. However, it was possible to utilise the potential dependent relative concentration of surface species, derived from the intensity of the VSFG signal, and the knowledge of the electrochemical stability of the possible intermediate species to demonstrate that the rate-determining step in catalysis in this case was unlikely to be the reduction of [Mn(bpy)(CO)$_4$]$^+$.

The potential dependence of the intensity of the VSFG responses of electrochemically generated species during the reduction of [Mn(bpy)(CO)$_3$(CH$_3$CN)]$^+$ also provided an insight into how the VSFG signal arises can be obtained from our nominally "solution" molecular electrocatalyst, Fig. 13.[25] Using the square root of I_{SFG} as an estimation of the relative concentration of the SFG it was concluded that if the electrochemical cell was left to return to open circuit only a low concentration of catalyst was present at the electrode surface. Upon application of a positive potential to the Au/Hg the intensity of the ν(CO) modes assigned to [Mn(bpy)(CO)$_3$(CH$_3$CN)]$^+$ increased, likely due to the increased electric field leading to ordering of the complex at, or close to the electrode surface (*i.e.* within the EDL). As [Mn(bpy)(CO)$_3$(CH$_3$CN)]$^+$ was reduced (−0.6 V) we found that the signal of [Mn$_2$(bpy)$_2$(CO)$_6$] increased before being reduced itself (−1.1 V). Clearly, Fig. 13 shows that it is possible to follow the build-up of an ordered population of the complex in the presence of the electric field, but it does not resolve the question of if the complex is adsorbed onto the electrode surface itself, or if it remains in the solution but within the EDL. To address this question here we have compared the measured SFG intensities to the current recorded *in situ*.

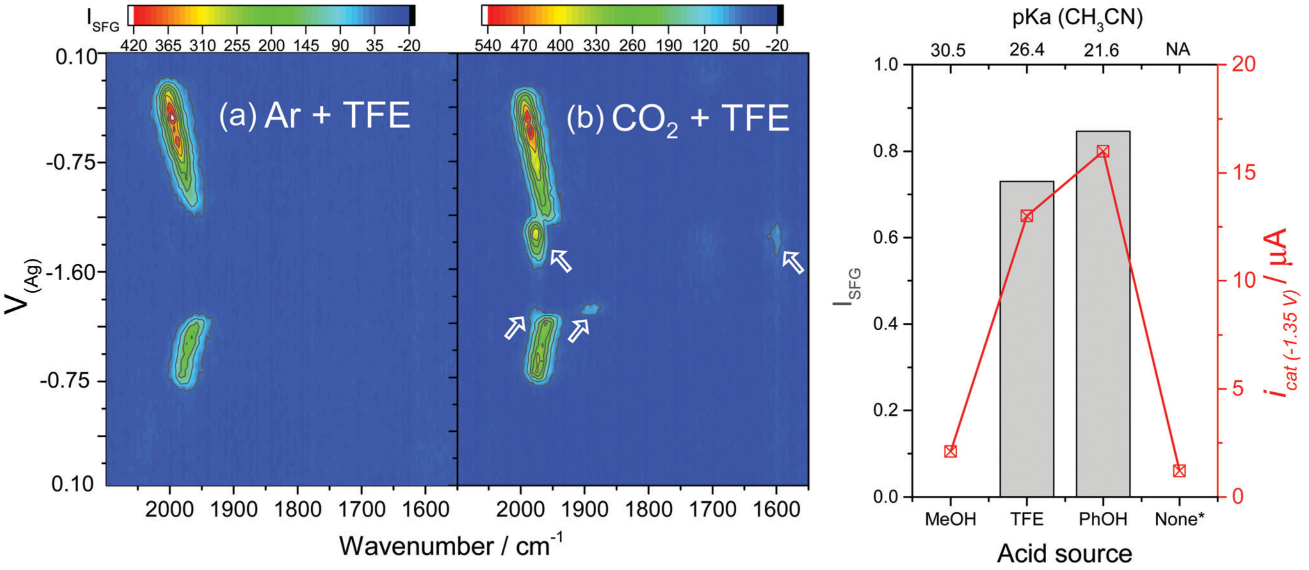

Fig. 12 (a) Potential dependent VSFG spectra of [Mn(bpy)(CO)$_3$Br] in CH$_3$CN and 0.1 M trifluoroethanol under Ar and (b) under CO$_2$. The arrows indicate new VSFG bands assignable to catalytic intermediates. (c) The intensity of the catalytic intermediate VSFG bands are found to correlate to the CO$_2$ reduction current and the pK_a of the acid used. Figure reproduced with permission from ref. 24.

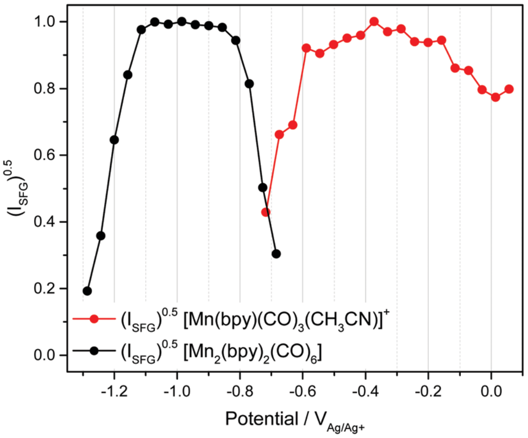

Fig. 13 Square root of the VSFG bands assigned to [Mn(bpy)(CO)$_3$(CH$_3$CN)]$^+$ (red) and [Mn$_2$(bpy)$_2$(CO)$_6$] (black), under Ar in the presence of 1.5 M TFE, are used to estimate surface concentrations during *in situ* measurement during a linear sweep voltammogram recorded at 10 mV s^{-1}. Figure reproduced with permission from ref. 25.

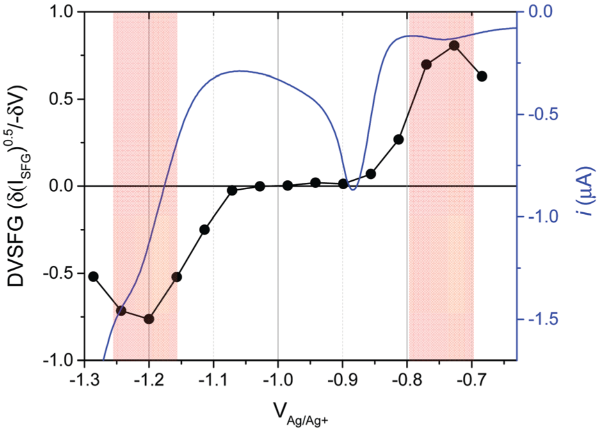

Fig. 14 Plot of the first differential of the $I_{SFG}^{0.5}$ of the VSFG band assigned to [Mn$_2$(bpy)$_2$(CO)$_6$] black (left axis) recorded during a linear sweep voltammogram at 10 mV s^{-1} provides a measure of the rate of formation/loss of the complex that is directly comparable to the current (i)–voltage data recorded at the same time. The red boxes highlight that although the greatest rate of [Mn$_2$(bpy)$_2$(CO)$_6$] loss as detected by VSFG corresponds to the diffusion limited peak in the i–V curve assignable to [Mn$_2$(bpy)$_2$(CO)$_6$] reduction (−1.2 V), the rate of formation of the VSFG detectable population of [Mn$_2$(bpy)$_2$(CO)$_6$] does not correspond to the diffusion limited bulk reduction of [Mn(bpy)(CO)$_3$(CH$_3$CN)]$^+$ at −0.9 V, instead a small surface population that is reduced at −0.75 V gives rise to the VSFG signal.

Differential cyclic voltabsorptometry has been used to correlate changes in optical absorption spectra to measured currents during cyclic voltamogramms.[140] The derivative of the measured absorption change in a spectroelectrochemical experiment provides a measure of the rate of change of concentration of the species being formed or removed electrochemically and hence it can be directly compared to the current (a rate measurement) in the current–voltage plot. The maxima/minima in the differential spectral data should occur at the same potentials as the peak in the current–voltage plot for the process being followed. Here we have reanalysed SFG data recorded during a linear sweep voltamogramm in the voltage region where [Mn$_2$(bpy)$_2$(CO)$_6$] is generated and destroyed to construct a differential voltammetric VSFG (DV-VSFG) plot, Fig. 14. The differential of the square route of the intensity of the SFG peak assigned to [Mn$_2$(bpy)$_2$(CO)$_6$] shows a clear maxima at −0.75 V and a minima at −1.20 V. The current–voltage plot shown has been analysed in detail elsewhere[24,25] and the peak at −0.89 V is assigned to the diffusion limited reduction of [Mn(bpy)(CO)$_3$(CH$_3$CN)]$^+$ to form the dimer complex and it is clear that the maxima of the DVSFG plot does not correlate with this electrochemical feature. Instead we find the DV-VSFG maxima at −0.75 V matches a smaller reduction seen in the linear sweep voltammetry that electrochemical measurements indicate is due to the reduction of surface adsorbed [Mn(bpy)(CO)$_3$(CH$_3$CN)]$^+$. Therefore in the studies of [Mn(bpy)(CO)$_3$(CH$_3$CN)]$^+$ on Hg/Au it appears that several of the species observed are likely to be transiently adsorbed onto the electrode surface.[25]

4 Outlook

The experiments to date on [Mn(bpy)(CO)$_3$CH$_3$CN]$^+$ and [Mo(bpy)(CO)$_4$] demonstrate the prospective of VSFG to study short-lived intermediates of molecular catalysis at an electrode surface and the remarkable potential of VSFG to rationalise current–voltage sweep measurements in real time. However to become wide spread as a technique it will be necessary to move beyond catalysts that adsorb directly to the electrode surface. Indeed VSFG studies in our laboratory are now focussed on exploring if the short-lived ordered structures of non-adsorbed catalysts within the EDL during electrocatalysis are detectable. Early results are promising. In-line with these observations is that [Mo(bpy)(CO)$_4$] could be measured by VSFG at Pt,[154] an electrode material which the complex does not strongly interact with, and the findings of Kubiak and co-workers who saw strong VSFG responses at potentials negative of where the reductive desorption of thiolated Mn and Re complexes on Au occurs.[142]

The VSFG studies to date on heterogeneous electrocatalytic oxidation mechanisms outlined above also further reinforce the ability of the technique to resolve remarkable levels of detail, even when studying complex mechanisms. As the field continues to mature we anticipate further advances, likely through the application of PS-VSFG measurements to electrode surfaces under potentiostatic control, a challenging but now realistically achievable goal. Such measurements will be critical if we are to address perhaps the most important reaction mechanism in sustainable fuels chemistry, the oxidation of water. For over 40 years the mechanisms of water oxidation at oxide electrodes and photoelectrodes has been debated[161] and the unique capability of VSFG spectroscopy to directly probe the electrode–electrolyte interface *in situ* appears to be a powerful tool to address the debate.

Conflicts of interest

There are no conflicts to declare.

Acknowledgements

AJC and AMG thank the EPSRC for funding (EP/K006851/1, EP/P034497/1). KHS acknowledges the University of Liverpool for a studentship. Dr Paul M. Donaldson (STFC) is thanked for insightful discussions throughout the VSFG adventure.

Notes and references

1 M. G. Walter, *et al.*, Solar Water Splitting Cells, *Chem. Rev.*, 2010, **110**, 6446–6473.

2 C. Costentin, M. Robert and J. M. Savéant, Catalysis of the electrochemical reduction of carbon dioxide, *Chem. Soc. Rev.*, 2013, **42**, 2423–2436.

3 M. E. Dry, The Fischer–Tropsch process: 1950–2000, *Catal. Today*, 2002, **71**, 227–241.

4 P. L. Stiles, J. A. Dieringer, N. C. Shah and R. P. Van Duyne, Surface-Enhanced Raman Spectroscopy, *Annu. Rev. Anal. Chem.*, 2008, **1**, 601–626.

5 F. Neubrech, C. Huck, K. Weber, A. Pucci and H. Giessen, Surface-Enhanced Infrared Spectroscopy Using Resonant Nanoantennas, *Chem. Rev.*, 2017, **117**, 5110–5145.

6 Y. R. Shen, *The principles of nonlinear optics*, Wiley, New York, 1984.

7 A. G. Lambert, P. B. Davies and D. J. Neivandt, Implementing the Theory of Sum Frequency Generation Vibrational Spectroscopy: A Tutorial Review, *Appl. Spectrosc. Rev.*, 2005, **40**, 103–145.

8 R. L. York, Y. Li, G. J. Holinga and G. A. Somorjai, Sum frequency generation vibrational spectra: the influence of experimental geometry for an absorptive medium or media, *J. Phys. Chem. A*, 2009, **113**, 2768–2774.

9 R. Feng, Y. Guo, R. Lü, L. Velarde and H. Wang, Consistency in the Sum Frequency Generation Intensity and Phase Vibrational Spectra of the Air/Neat Water Interface, *J. Phys. Chem. A*, 2011, **115**, 6015–6027.

10 A. G. Lambert, D. J. Neivandt, A. M. Briggs, E. W. Usadi and P. B. Davies, Interference Effects in Sum Frequency Spectra from Monolayers on Composite Dielectric/Metal Substrates, *J. Phys. Chem. B*, 2002, **106**, 5461–5469.

11 Y. Tong, *et al.*, Interference effects in the sum frequency generation spectra of thin organic films. I. Theoretical modeling and simulation, *J. Chem. Phys.*, 2010, **133**, 034704.

12 Y. Tong, *et al.*, Interference effects in the sum frequency generation spectra of thin organic films. II: applications to different thin-film systems, *J. Chem. Phys.*, 2010, **133**, 034705.

13 G. Li, A. Dhinojwala and M. S. Yeganeh, Interference Effect from Buried Interfaces Investigated by Angular-Dependent Infrared−Visible Sum Frequency Generation Technique, *J. Phys. Chem. C*, 2011, **115**, 7554–7561.

14 X. Lu, *et al.*, A Sum Frequency Generation Vibrational Study of the Interference Effect in Poly(*n*-butyl methacrylate) Thin Films Sandwiched between Silica and Water, *J. Phys. Chem. C*, 2011, **115**, 13759–13767.

15 E. H. G. Backus, N. Garcia-Araez, M. Bonn and H. J. Bakker, On the role of fresnel factors in sum-frequency generation spectroscopy of metal-water and metal-oxide-water interfaces, *J. Phys. Chem. C*, 2012, **116**, 23351–23361.

16 A. G. Lambert, P. B. Davies and D. J. Neivandt, Implementing the theory of sum frequency generation vibrational spectroscopy: a tutorial review, *Appl. Spectrosc. Rev.*, 2005, **40**, 103–145.

17 N. G. Rey and D. D. Dlott, Studies of electrochemical interfaces by broadband sum frequency generation, *J. Electroanal. Chem.*, 2017, **800**, 114–125.

18 X. D. Zhu, H. Suhr and Y. R. Shen, Surface vibrational spectroscopy by infrared-visible sum frequency generation, *Phys. Rev. B: Condens. Matter Mater. Phys.*, 1987, **35**, 3047–3050.

19 P. Guyot-Sionnest and A. Tadjeddine, Spectroscopic investigations of adsorbates at the metal-electrolyte interface using sum frequency generation, *Chem. Phys. Lett.*, 1990, **172**, 341–345.

20 L. J. Richter, T. P. Petralli-Mallow and J. C. Stephenson, Vibrationally resolved sum-frequency generation with broad-bandwidth infrared pulses, *Opt. Lett.*, 1998, **23**, 1594.

21 A. Ge, *et al.*, Interfacial Structure and Electric Field Probed by *in situ* Electrochemical Vibrational Stark Effect Spectroscopy and Computational Modeling, *J. Phys. Chem. C*, 2017, **121**, 18674–18682.

22 A. Lagutchev, S. A. Hambir and D. D. Dlott, Nonresonant background suppression in broadband vibrational sum-frequency generation spectroscopy, *J. Phys. Chem. C*, 2007, **111**, 13645–13647.

23 G. Neri, P. M. Donaldson and A. J. Cowan, The Role of Electrode–Catalyst Interactions in Enabling Efficient CO_2 Reduction with $Mo(bpy)(CO)_4$ As Revealed by Vibrational Sum-Frequency Generation Spectroscopy, *J. Am. Chem. Soc.*, 2017, **139**, 13791–13797.

24 G. Neri, J. J. Walsh, G. Teobaldi, P. M. Donaldson and A. J. Cowan, Detection of catalytic intermediates at an electrode surface during carbon dioxide reduction by an earth-abundant catalyst, *Nat. Catal.*, 2018, **1**, 952–959.

25 G. Neri, P. M. Donaldson and A. J. Cowan, *In situ* study of the low overpotential ''dimer pathway'' for electrocatalytic carbon dioxide reduction by manganese carbonyl complexes, *Phys. Chem. Chem. Phys.*, 2019, **21**, 7389–7397.

26 N. Ji, V. Ostroverkhov, C. Y. Chen and Y. R. Shen, Phase-sensitive sum-frequency vibrational spectroscopy and its application to studies of interfacial alkyl chains, *J. Am. Chem. Soc.*, 2007, **129**, 10056–10057.

27 I. V. Stiopkin, H. D. Jayathilake, A. N. Bordenyuk and A. V. Benderskii, Heterodyne-detected vibrational sum frequency generation spectroscopy, *J. Am. Chem. Soc.*, 2008, **130**, 2271–2275.

28 R. E. Pool, J. Versluis, E. H. G. Backus and M. Bonn, Comparative study of direct and phase-specific vibrational sum-frequency generation spectroscopy: advantages and limitations, *J. Phys. Chem. B*, 2011, **115**, 15362–15369.

29 H. Vanselous and P. B. Petersen, Extending the Capabilities of Heterodyne-Detected Sum-Frequency Generation

Spectroscopy: probing Any Interface in Any Polarization Combination, *J. Phys. Chem. C*, 2016, **120**, 8175–8184.

30 S. Yamaguchi and T. Tahara, Heterodyne-detected electronic sum frequency generation: 'Up' *versus* 'down' alignment of interfacial molecules, *J. Chem. Phys.*, 2008, **129**, 064201.

31 J. Wang, P. J. Bisson, J. M. Marmolejos and M. J. Shultz, Nonlinear interferometer: design, implementation, and phase-sensitive sum frequency measurement, *J. Chem. Phys.*, 2017, **147**, 101102.

32 J. Wang, P. J. Bisson, J. M. Marmolejos and M. J. Shultz, Measuring Complex Sum Frequency Spectra with a Nonlinear Interferometer, *J. Phys. Chem. Lett.*, 2016, **7**, 1945–1949.

33 S. Sun, P. J. Bisson, M. Bonn, M. J. Shultz and E. H. G. Backus, Phase-Sensitive Sum-Frequency Generation Measurements Using a Femtosecond Nonlinear Interferometer, *J. Phys. Chem. C*, 2019, **123**, 7266–7270.

34 S. Yang, H. Noguchi and K. Uosaki, Electronic Structure of the CO/Pt(111) Electrode Interface Probed by Potential-Dependent IR/Visible Double Resonance Sum Frequency Generation Spectroscopy, *J. Phys. Chem. C*, 2015, **119**, 26056–26063.

35 P. S. Bagus, C. J. Nelin, K. Hermann and M. R. Philpott, Coupling of vibrational modes of adsorbates: application to field-induced shifts for CO and CN on Cu(100), *Phys. Rev. B: Condens. Matter Mater. Phys.*, 1987, **36**, 8169–8172.

36 K. Kunimatsu, H. Seki, W. G. Golden, J. G. Gordon and M. R. Philpott, Carbon monoxide adsorption on a platinum electrode studied by polarization-modulated FT-IR reflection-absorption spectroscopy: II. Carbon monoxide adsorbed at a potential in the hydrogen region and its oxidation in acids, *Langmuir*, 1986, **2**, 464–468.

37 W. Daum, *et al.*, Sum-frequency generation at electrochemical interfaces: cyanide vibrations on Pt(111) and Pt(110), *Appl. Phys. A: Solids Surf.*, 1994, **59**, 553–562.

38 A. Tadjeddine, *et al.*, Investigation of the vibrational properties of CN – on a Pt electrode by *in situ* VIS–IR sum frequency generation and functional density calculations, *J. Chem. Soc., Faraday Trans.*, 1996, **92**, 3823–3828.

39 M. Tadjeddine, J. P. Flament, A. Le Rille and A. Tadjeddine, SFG experiment and *ab initio* study of the chemisorption of CN- on low-index platinum surfaces, *Surf. Sci.*, 2006, **600**, 2138–2153.

40 A. Tadjeddine, A. Peremans and P. Guyot-Sionnest, Vibrational spectroscopy of the electrochemical interface by visible-infrared sum-frequency generation, *Surf. Sci.*, 1995, **335**, 210–220.

41 A. Le Rille, A. Tadjeddine, W. Q. Zheng and A. Peremans, Vibrational spectroscopy of a Au(*hkl*)-electrolyte interface by *in situ* visible-infrared difference frequency generation, *Chem. Phys. Lett.*, 1997, **271**, 95–100.

42 A. Le Rille and A. Tadjeddine, *In situ* visible-infrared sum and difference frequency generation at the electrochemical interface, *J. Electroanal. Chem.*, 1999, **467**, 238–248.

43 A. Tadjeddine and A. Le Rille, Adsorption of cyanide on gold single crystal investigated by *in situ* visible-infrared difference frequency generation, *Electrochim. Acta*, 1999, **45**, 601–609.

44 C. Rambaud, L. Cagnon, J.-P. Levy and G. Tourillon, SFG Study of Thiocyanate Ion Adsorption onto Polycrystalline Au Electrode and Electrodeposited Metallic Thin Films, *J. Electrochem. Soc.*, 2004, **151**, E352.

45 F. Vidal and A. Tadjeddine, Sum-frequency generation spectroscopy of interfaces, *Rep. Prog. Phys.*, 2005, **68**, 1095–1127.

46 A. Peremans and A. Tadjeddine, Spectroscopic investigation of Pt-methanol interface in perchloric acid medium by sum-frequency generation, *Chem. Phys. Lett.*, 1994, **220**, 481–485.

47 A. Peremans and A. Tadjeddine, Spectroscopic investigation of electrochemical interfaces at overpotential by infrared-visible sum-frequency generation: platinum in base and methanol-containing electrolyte, *J. Electroanal. Chem.*, 1995, **395**, 313–316.

48 F. Vidal, *et al.*, The influence of surface defects in methanol dissociative adsorption and CO oxidation on Pt(110) probed by nonlinear vibrational SFG spectroscopy, *J. Electroanal. Chem.*, 2012, **672**, 1–6.

49 F. Vidal, *et al.*, Methanol dissociative adsorption on Pt(100) as studied by nonlinear vibrational spectroscopy, *J. Electroanal. Chem.*, 2004, **563**, 9–14.

50 F. Vidal, B. Busson, C. Six, O. Pluchery and A. Tadjeddine, SFG study of methanol dissociative adsorption at Pt(100), Pt(110) and Pt(111) electrodes surfaces, *Surf. Sci.*, 2002, **502–503**, 485–489.

51 O. Pluchery, M. Tadjeddine, J.-P. Flament and A. Tadjeddine, Adsorption of 4-cyanopyridine on Au(111): *ab initio* calculations and SFG measurements, *Phys. Chem. Chem. Phys.*, 2001, **3**, 3343–3350.

52 C. Romero and S. Baldelli, Sum frequency generation study of the room-temperature ionic liquids/quartz interface, *J. Phys. Chem. B*, 2006, **110**, 6213–6223.

53 Z. D. Schultz, M. E. Biggin, J. O. White and A. A. Gewirth, Infrared-Visible Sum Frequency Generation Investigation of Cu Corrosion Inhibition with Benzotriazole, *Anal. Chem.*, 2004, **76**, 604–609.

54 P. Hébert, A. Le Rille, W. Q. Zheng and A. Tadjeddine, Vibrational spectroscopic study of the adsorption of pyridine at the Au(111)-electrolyte interface by *in situ* difference frequency generation, *J. Electroanal. Chem.*, 1998, **447**, 5–9.

55 J. Kim, K. C. Chou and G. A. Somorjai, Investigations of the Potential-Dependent Structure of Phenylalanine on the Glassy Carbon Electrode by Infrared-Visible Sum Frequency Generation, *J. Phys. Chem. B*, 2002, **106**, 9198–9200.

56 C. Humbert, *et al.*, Sum-frequency generation as a vibrational and electronic probe of the electrochemical interface and thin films, *J. Electroanal. Chem.*, 2008, **621**, 314–321.

57 S. K. Shaw, A. Lagutchev, D. D. Dlott and A. A. Gewirth, Electrochemically driven reorientation of three ionic states of p-aminobenzoic acid on Ag(111), *J. Phys. Chem. C*, 2009, **113**, 2417–2424.

58 Z. D. Schultz, S. K. Shaw and A. A. Gewirth, Potential dependent organization of water at the electrified metal-liquid interface, *J. Am. Chem. Soc.*, 2005, **127**, 15916–15922.

59 N. García Rey and D. D. Dlott, Structural Transition in an Ionic Liquid Controls CO_2 Electrochemical Reduction, *J. Phys. Chem. C*, 2015, **119**, 20892–20899.

60 N. García Rey and D. D. Dlott, Effects of water on low-overpotential CO_2 reduction in ionic liquid studied by sum-frequency generation spectroscopy, *Phys. Chem. Chem. Phys.*, 2017, **19**, 10491–10501.

61 B. Braunschweig, P. Mukherjee, J. L. Haan and D. D. Dlott, Vibrational sum-frequency generation study of the CO_2 electrochemical reduction at Pt/EMIM-BF4 solid/liquid interfaces, *J. Electroanal. Chem.*, 2017, **800**, 144–150.

62 N. Garcia Rey and D. D. Dlott, Interrogating a Deeply Buried Electrode by Vibrational Sum Frequency Spectroscopy. Towards Understanding the Electroreduction at Ionic Liquid-Metal Interfaces, *ECS Trans.*, 2015, **66**, 21–31.

63 R. M. Hammaker, S. A. Francis and R. P. Eischens, Infrared study of intermolecular interactions for carbon monoxide chemisorbed on platinum, *Spectrochim. Acta*, 1965, **21**, 1295–1309.

64 J. H. K. Pfisterer, U. E. Zhumaev, W. Cheuquepan, J. M. Feliu and K. F. Domke, Stark effect or coverage dependence? Disentangling the EC-SEIRAS vibrational shift of sulfate on Au(111), *J. Chem. Phys.*, 2018, **150**, 041709.

65 P. Zhang, Y. Wei, J. Cai, Y.-X. Chen and Z.-Q. Tian, Nonlinear Stark effect observed for carbon monoxide chemisorbed on gold core/palladium shell nanoparticle film electrodes, using *in situ* surface-enhanced Raman spectroscopy, *Chin. J. Catal.*, 2016, **37**, 1156–1165.

66 B. Braunschweig, *et al.*, Spectroscopy of Electrified Interfaces with Broadband Sum Frequency Generation: from Electrocatalysis to Protein Foams, *Vibrational Spectroscopy at Electrified Interfaces*, Wiley Online Books, 2013, DOI: 10.1002/9781118658871.ch4.

67 J. F. Gomes, B. Busson, A. Tadjeddine and G. Tremiliosi-Filho, Ethanol electro-oxidation over Pt(*hkl*): comparative study on the reaction intermediates probed by FTIR and SFG spectroscopies, *Electrochim. Acta*, 2008, **53**, 6899–6905.

68 J. F. Gomes, B. Busson and A. Tadjeddine, SFG Study of the Ethanol in an Acidic Medium-Pt(110) Interface: effects of the Alcohol Concentration, *J. Phys. Chem. B*, 2006, **110**, 5508–5514.

69 A. Lagutchev, G. Q. Lu, T. Takeshita, D. D. Dlott and A. Wieckowski, Vibrational sum frequency generation studies of the $(2 \times 2) \rightarrow (\sqrt{19} \times \sqrt{19})$ phase transition of CO on Pt(111) electrodes, *J. Chem. Phys.*, 2006, **125**, 154705.

70 R. B. Kutz, *et al.*, Reaction pathways of ethanol electrooxidation on polycrystalline platinum catalysts in acidic electrolytes, *J. Catal.*, 2011, **278**, 181–188.

71 J. F. Gomes, K. Bergamaski, M. F. S. Pinto and P. B. Miranda, Reaction intermediates of ethanol electrooxidation on platinum investigated by SFG spectroscopy, *J. Catal.*, 2013, **302**, 67–82.

72 S. Dewan, D. Raciti, Y. Liu, D. H. Gracias and C. Wang, Comparative Studies of Ethanol and Ethylene Glycol Oxidation on Platinum Electrocatalysts, *Top. Catal.*, 2018, **0**, 0.

73 M. A. Brown, A. Goel and Z. Abbas, Effect of Electrolyte Concentration on the Stern Layer Thickness at a Charged Interface, *Angew. Chem., Int. Ed.*, 2016, **55**, 3790–3794.

74 S. Pezzotti, D. R. Galimberti, Y. R. Shen and M. P. Gaigeot, Structural definition of the BIL and DL: a new universal methodology to rationalize non-linear: $\chi^{(2)}(\omega)$ SFG signals at charged interfaces, including $\chi^{(3)}(\omega)$ contributions, *Phys. Chem. Chem. Phys.*, 2018, **20**, 5190–5199.

75 K. C. Jena, P. A. Covert and D. K. Hore, The effect of salt on the water structure at a charged solid surface: differentiating second- and third-order nonlinear contributions, *J. Phys. Chem. Lett.*, 2011, **2**, 1056–1061.

76 A. M. Darlington, T. A. Jarisz, E. L. Dewalt-Kerian, S. Roy, S. Kim, M. S. Azam, D. K. Hore and J. M. Gibbs, Separating the pH-Dependent Behavior of Water in the Stern and Diffuse Layers with Varying Salt Concentration, *J. Phys. Chem. C*, 2017, **121**, 20229–20241.

77 T. Joutsuka and A. Morita, Electrolyte and Temperature Effects on Third-Order Susceptibility in Sum Frequency Generation Spectroscopy of Aqueous Salt Solutions, *J. Phys. Chem. C*, 2018, **122**, 11407–11413.

78 C. Schnitzer, S. Baldelli and M. J. Shultz, Sum Frequency Generation of Water on NaCl, $NaNO_3$, $KHSO_4$, HCl, HNO_3, and H_2SO_4 Aqueous Solutions, *J. Phys. Chem. B*, 2000, **104**, 585–590.

79 K. C. Jena and D. K. Hore, Variation of Ionic Strength Reveals the Interfacial Water Structure at a Charged Mineral Surface, *J. Phys. Chem. C*, 2009, **113**, 15364–15372.

80 P. E. Ohno, H. F. Wang and F. M. Geiger, Second-order spectral lineshapes from charged interfaces, *Nat. Commun.*, 2017, **8**, 1–9.

81 K. A. Lovering, A. K. Bertram and K. C. Chou, New Information on the Ion-Identity-Dependent Structure of Stern Layer Revealed by Sum Frequency Generation Vibrational Spectroscopy, *J. Phys. Chem. C*, 2016, **120**, 18099–18104.

82 Y. R. Shen and V. Ostroverkhov, Sum-frequency vibrational spectroscopy on water interfaces: polar orientation of water molecules at interfaces, *Chem. Rev.*, 2006, **106**, 1140–1154.

83 L. Zhang, C. Tian, G. A. Waychunas and Y. R. Shen, Structures and charging of α-alumina (0001)/water interfaces studied by sum-frequency vibrational spectroscopy, *J. Am. Chem. Soc.*, 2008, **130**, 7686–7694.

84 M. P. Gaigeot, M. Sprik and M. Sulpizi, Oxide/water interfaces: how the surface chemistry modifies interfacial water properties, *J. Phys.: Condens. Matter*, 2012, **24**, 124106.

85 S. Schrödle, F. G. Moore and G. L. Richmond, Surface speciation at solid/liquid interfaces: a vibrational sum-frequency study of acetate adsorption at the fluorite/water interface, *J. Phys. Chem. C*, 2007, **111**, 10088–10094.

86 K. A. Becraft and G. L. Richmond, *In situ* vibrational spectroscopic studies of the CaF_2/H_2O interface, *Langmuir*, 2001, **17**, 7721–7724.

87 V. Ostroverkhov, G. A. Waychunas and Y. R. Shen, Vibrational spectra of water at water/α-quartz (0001) interface, *Chem. Phys. Lett.*, 2004, **386**, 144–148.

88 Q. Du, E. Freysz and Y. R. Shen, Vibrational spectra of water molecules at quartz/water interfaces, *Phys. Rev. Lett.*, 1994, **72**, 238–241.

89 E. Tyrode and J. F. D. Liljeblad, Water structure next to ordered and disordered hydrophobic silane monolayers: a vibrational sum frequency spectroscopy study, *J. Phys. Chem. C*, 2013, **117**, 1780–1790.

90 O. Isaienko and E. Borguet, Hydrophobicity of hydroxylated amorphous fused silica surfaces, *Langmuir*, 2013, **29**, 7885–7895.

91 V. Ostroverkhov, G. A. Waychunas and Y. R. Shen, New information on water interfacial structure revealed by phase-sensitive surface spectroscopy, *Phys. Rev. Lett.*, 2005, **94**, 2–5.

92 M. Sovago, *et al.*, Vibrational Response of Hydrogen-Bonded Interfacial Water is Dominated by Intramolecular Coupling, *Phys. Rev. Lett.*, 2008, **100**, 173901.

93 C. S. Tian and Y. R. Shen, Isotopic dilution study of the water/vapor interface by phase-sensitivesum-frequency vibrational spectroscopy, *J. Am. Chem. Soc.*, 2009, **131**, 2790–2791.

94 S. H. Urashima, A. Myalitsin, S. Nihonyanagi and T. Tahara, The Topmost Water Structure at a Charged Silica/Aqueous Interface Revealed by Heterodyne-Detected Vibrational Sum Frequency Generation Spectroscopy, *J. Phys. Chem. Lett.*, 2018, **9**, 4109–4114.

95 A. Myalitsin, S. H. Urashima, S. Nihonyanagi, S. Yamaguchi and T. Tahara, Water structure at the buried silica/aqueous interface studied by heterodyne-detected vibrational sum-frequency generation, *J. Phys. Chem. C*, 2016, **120**, 9357–9363.

96 S. Nihonyanagi, S. Yamaguchi and T. Tahara, Ultrafast Dynamics at Water Interfaces Studied by Vibrational Sum Frequency Generation Spectroscopy, *Chem. Rev.*, 2017, **117**, 10665–10693.

97 J. C. Deàk, S. T. Rhea, L. K. Iwaki and D. D. Dlott, Vibrational energy relaxation and spectral diffusion in water and deuterated water, *J. Phys. Chem. A*, 2000, **104**, 4866–4875.

98 M. A. Brown, *et al.*, Determination of surface potential and electrical double-layer structure at the aqueous electrolyte-nanoparticle interface, *Phys. Rev. X*, 2016, **6**, 1–12.

99 Y. C. Wen, *et al.*, Unveiling Microscopic Structures of Charged Water Interfaces by Surface-Specific Vibrational Spectroscopy, *Phys. Rev. Lett.*, 2016, **116**, 1–5.

100 C. Tian, N. Ji, G. A. Waychunas and Y. R. Shen, Interfacial Structures of Acidic and Basic Aqueous Solutions, *J. Am. Chem. Soc.*, 2008, **130**, 13033–13039.

101 C. Y. Wang, H. Groenzin and M. J. Shultz, Molecular species on nanoparticulate anatase TiO_2 film detected by sum frequency generation: trace hydrocarbons and hydroxyl groups, *Langmuir*, 2003, **19**, 7330–7334.

102 O. Isaienko, S. Nihonyanagi, D. Sil and E. Borguet, Observation of the bending mode of interfacial water at silica surfaces by near-infrared vibrational sum-frequency generation spectroscopy of the [stretch + bend] combination bands, *J. Phys. Chem. Lett.*, 2013, **4**, 531–535.

103 C. Dutta and A. V. Benderskii, On the Assignment of the Vibrational Spectrum of the Water Bend at the Air/Water Interface, *J. Phys. Chem. Lett.*, 2017, **8**, 801–804.

104 M. Vinaykin and A. V. Benderskii, Vibrational sum-frequency spectrum of the water bend at the air/water interface, *J. Phys. Chem. Lett.*, 2012, **3**, 3348–3352.

105 Y. Tong, T. Kampfrath and R. K. Campen, Experimentally probing the libration of interfacial water: the rotational potential of water is stiffer at the air/water interface than in bulk liquid, *Phys. Chem. Chem. Phys.*, 2016, **18**, 18424–18430.

106 Y. Tong, *et al.*, Optically probing Al-O and O-H vibrations to characterize water adsorption and surface reconstruction on α-alumina: an experimental and theoretical study, *J. Chem. Phys.*, 2015, **142**, 054704.

107 H. S. Alsalem, *et al.*, Characterisation, coverage, and orientation of functionalised graphene using sum-frequency generation spectroscopy, *Phys. Chem. Chem. Phys.*, 2018, **20**, 8962–8967.

108 S. Kataoka, *et al.*, Investigation of water structure at the TiO_2/aqueous interface, *Langmuir*, 2004, **20**, 1662–1666.

109 S. Hosseinpour, *et al.*, Chemisorbed and Physisorbed Water at the TiO_2/Water Interface, *J. Phys. Chem. Lett.*, 2017, **8**, 2195–2199.

110 K. Uosaki, T. Yano and S. Nihonyanagi, Interfacial Water Structure at As-Prepared and UV-Induced Hydrophilic TiO_2 Surfaces Studied by Sum Frequency Generation Spectroscopy and Quartz Crystal Microbalance, *J. Phys. Chem. B*, 2004, **108**, 19086–19088.

111 J. E. Bertie and Z. Lan, Infrared Intensities of Liquids XX: the Intensity of the OH Stretching Band of Liquid Water Revisited, and the Best Current Values of the Optical Constants of $H_2O(l)$ at 25 °C between 15 000 and 1 cm^{-1}, *Appl. Spectrosc.*, 1996, **50**, 1047–1057.

112 H. Noguchi, T. Okada and K. Uosaki, Molecular structure at electrode/electrolyte solution interfaces related to electrocatalysis, *Faraday Discuss.*, 2008, **140**, 125–137.

113 S. Nihonyanagi, *et al.*, Potential-dependent structure of the interfacial water on the gold electrode, *Surf. Sci.*, 2004, **573**, 11–16.

114 H. Noguchi, T. Okada and K. Uosaki, SFG study on potential-dependent structure of water at Pt electrode/electrolyte solution interface, *Electrochim. Acta*, 2008, **53**, 6841–6844.

115 D. Verreault, V. Kurz, C. Howell and P. Koelsch, Sample cells for probing solid/liquid interfaces with broadband sum-frequency-generation spectroscopy, *Rev. Sci. Instrum.*, 2010, **81**, 063111.

116 J. D. Benck, B. A. Pinaud, Y. Gorlin and T. F. Jaramillo, Substrate Selection for Fundamental Studies of Electrocatalysts and Photoelectrodes: inert Potential Windows in Acidic, Neutral, and Basic Electrolyte, *PLoS One*, 2014, **9**, e107942.

117 A. Peremans and A. Tadjeddine, Electrochemical deposition of hydrogen on platinum single crystals studied by infrared-visible sum-frequency generation, *J. Chem. Phys.*, 1995, **103**, 7197–7203.

118 A. Peremans and A. Tadjeddine, Vibrational Spectroscopy of Electrochemically Deposited Hydrogen on Platinum, *Phys. Rev. Lett.*, 1994, **73**, 3010–3013.

119 Y. Tong, Q. Peng, T. Ma, T. Nishida and S. Ye, Photocatalytic oxidation of the organic monolayers on TiO_2 surface investigated by *in situ* sum frequency generation spectroscopy, *APL Mater.*, 2015, **3**, 104402.

120 O. Diaz-Morales, D. Ferrus-Suspedra and M. T. M. Koper, The importance of nickel oxyhydroxide deprotonation on its activity towards electrochemical water oxidation, *Chem. Sci.*, 2016, **7**, 2639–2645.

121 M. Zhang, M. de Respinis and H. Frei, Time-resolved observations of water oxidation intermediates on a cobalt oxide nanoparticle catalyst, *Nat. Chem.*, 2014, **6**, 362–367.

122 Y. Zhang, *et al.*, Rate-Limiting O-O Bond Formation Pathways for Water Oxidation on Hematite Photoanode, *J. Am. Chem. Soc.*, 2018, **140**, 3264–3269.

123 O. Zandi and T. W. Hamann, Determination of photoelectrochemical water oxidation intermediates on haematite electrode surfaces using operando infrared spectroscopy, *Nat. Chem.*, 2016, **8**, 778–783.

124 X. Chen, *et al.*, The formation time of Ti-O$^\bullet$ and Ti-O$^\bullet$-Ti radicals at the n-$SrTiO_3$/aqueous interface during photocatalytic water oxidation, *J. Am. Chem. Soc.*, 2017, **139**, 1830–1841.

125 D. M. Herlihy, *et al.*, Detecting the oxyl radical of photocatalytic water oxidation at an n-$SrTiO_3$/aqueous interface through its subsurface vibration, *Nat. Chem.*, 2016, **8**, 549–555.

126 N. Sivasankar, W. W. Weare and H. Frei, Direct observation of a hydroperoxide surface intermediate upon visible light-driven water oxidation at an Ir oxide nanocluster catalyst by rapid-scan FT-IR spectroscopy, *J. Am. Chem. Soc.*, 2011, **133**, 12976–12979.

127 Z. Pavlovic, C. Ranjan, M. van Gastel and R. Schlögl, The active site for the water oxidising anodic iridium oxide probed through *in situ* Raman spectroscopy, *Chem. Commun.*, 2017, **53**, 12414–12417.

128 V. Pfeifer, *et al.*, *In situ* observation of reactive oxygen species forming on oxygen-evolving iridium surfaces, *Chem. Sci.*, 2017, **8**, 2143–2149.

129 PNNL centre for molecular electrocatalysis, glossary pages.

130 A. Dey, The Way Forward in Molecular Electrocatalysis, *Inorg. Chem.*, 2016, **55**, 10831–10834.

131 K. J. Lee, N. Elgrishi, B. Kandemir and J. L. Dempsey, Electrochemical and spectroscopic methods for evaluating molecular electrocatalysts, *Nat. Rev. Chem.*, 2017, **1**, 0039.

132 C. L. Anfuso, *et al.*, Covalent Attachment of a Rhenium Bipyridyl CO_2 Reduction Catalyst to Rutile TiO_2, *J. Am. Chem. Soc.*, 2011, **133**, 6922–6925.

133 C. L. Anfuso, *et al.*, Orientation of a Series of CO_2 Reduction Catalysts on Single Crystal TiO_2 Probed by Phase-Sensitive Vibrational Sum Frequency Generation Spectroscopy (PS-VSFG), *J. Phys. Chem. C*, 2012, **116**, 24107–24114.

134 A. Ge, *et al.*, Surface-Induced Anisotropic Binding of a Rhenium CO_2-Reduction Catalyst on Rutile TiO_2(110) Surfaces, *J. Phys. Chem. C*, 2016, **120**, 20970–20977.

135 C. L. Anfuso, A. M. Ricks, W. Rodríguez-Córdoba and T. Lian, Ultrafast Vibrational Relaxation Dynamics of a Rhenium Bipyridyl CO_2 Reduction Catalyst at a Au Electrode Surface Probed by Time-Resolved Vibrational Sum Frequency Generation Spectroscopy, *J. Phys. Chem. C*, 2012, **116**, 26377–26384.

136 M. L. Clark, *et al.*, Orientation of Cyano-Substituted Bipyridine Re(I) *fac*-Tricarbonyl Electrocatalysts Bound to Conducting Au Surfaces, *J. Phys. Chem. C*, 2016, **120**, 1657–1665.

137 J. Wang, *et al.*, Short-Range Catalyst-Surface Interactions Revealed by Heterodyne Two-Dimensional Sum Frequency Generation Spectroscopy, *J. Phys. Chem. Lett.*, 2015, **6**, 4204–4209.

138 C. Calabrese, H. Vanselous and P. B. Petersen, Deconstructing the Heterogeneity of Surface-Bound Catalysts: Rutile Surface Structure Affects Molecular Properties, *J. Phys. Chem. C*, 2016, **120**, 1515–1522.

139 H. Vanselous, A. M. Stingel and P. B. Petersen, Interferometric 2D Sum Frequency Generation Spectroscopy Reveals Structural Heterogeneity of Catalytic Monolayers on Transparent Materials, *J. Phys. Chem. Lett.*, 2017, **8**, 825–830.

140 J. J. Walsh, *et al.*, Directing the mechanism of CO_2 reduction by a Mn catalyst through surface immobilization, *Phys. Chem. Chem. Phys.*, 2018, **20**, 6811–6816.

141 G. Boschloo and D. Fitzmaurice, Electron Accumulation in Nanostructured TiO_2 (Anatase) Electrodes, *J. Phys. Chem. B*, 1999, **103**, 7860–7868.

142 M. L. Clark, *et al.*, CO_2 Reduction Catalysts on Gold Electrode Surfaces Influenced by Large Electric Fields, *J. Am. Chem. Soc.*, 2018, **140**, 17643–17655.

143 F. C. Anson, Chronopotentiometry of Iron(II) and Iron(III) Adsorbed on Platinum Electrodes, *Anal. Chem.*, 1961, **33**, 1498–1502.

144 Y. Horowitz, H.-L. Han and G. A. Somorjai, Identifying the Decomposition of Diethyl Carbonate in Binary Electrolyte Solutions in Contact with Silicon Anodes – A Sum Frequency Generation Vibrational Spectroscopy Study, *Ind. Eng. Chem. Res.*, 2018, **57**, 1480–1486.

145 Y. Horowitz, H. L. Han, P. N. Ross and G. A. Somorjai, *In Situ* Potentiodynamic Analysis of the Electrolyte/Silicon Electrodes Interface Reactions – A Sum Frequency Generation Vibrational Spectroscopy Study, *J. Am. Chem. Soc.*, 2016, **138**, 726–729.

146 G. B. Balazs and F. C. Anson, Effects of CO on the electrocatalytic activity of Ni(cyclam)$^{2+}$ toward the reduction of CO_2, *J. Electroanal. Chem.*, 1993, **361**, 149–157.

147 J. Tory, B. Setterfield-Price, R. A. W. Dryfe and F. Hartl, [M(CO)$_4$ (2,2′-bipyridine)] (M = Cr, Mo, W) Complexes as Efficient Catalysts for Electrochemical Reduction of CO_2 at a Gold Electrode, *ChemElectroChem*, 2015, **2**, 213–217.

148 Y. Wu, *et al.*, Electrode-Ligand Interactions Dramatically Enhance CO_2 Conversion to CO by the [Ni(cyclam)](PF$_6$)$_2$ Catalyst, *ACS Catal.*, 2017, **7**, 5282–5288.

149 J. E. Pander, M. F. Baruch and A. B. Bocarsly, Probing the Mechanism of Aqueous CO_2 Reduction on Post-Transition-Metal Electrodes using ATR-IR Spectroelectrochemistry, *ACS Catal.*, 2016, **6**, 7824–7833.

150 M. L. Clark, K. A. Grice, C. E. Moore, A. L. Rheingold and C. P. Kubiak, Electrocatalytic CO_2 reduction by M(bpy-R)(CO)$_4$

(M = Mo, W; R = H, *t*Bu) complexes. Electrochemical, spectroscopic, and computational studies and comparison with group 7 catalysts, *Chem. Sci.*, 2014, **5**, 1894–1900.

151 J. O. Taylor, R. D. Leavey and F. Hartl, Solvent and Ligand Substitution Effects on the Electrocatalytic Reduction of CO_2 with [Mo(CO)$_4$ (x,x'-dimethyl-2,2′-bipyridine)] (x =4–6) Enhanced at a Gold Cathodic Surface, *ChemElectroChem*, 2018, **5**, 3155–3161.

152 K. A. Grice and C. Saucedo, Electrocatalytic Reduction of CO_2 by Group 6 M(CO)$_6$ Species without ''Non-Innocent'' Ligands, *Inorg. Chem.*, 2016, **55**, 6240–6246.

153 F. Franco, *et al.*, Electrochemical Reduction of CO_2 by M(CO) 4 (diimine) Complexes (M = Mo, W): Catalytic Activity Improved by 2,2′-Dipyridylamine, *ChemElectroChem*, 2015, **2**, 1372–1379.

154 G. Neri, P. M. Donaldson and A. J. Cowan, The Role of Electrode–Catalyst Interactions in Enabling Efficient CO_2 Reduction with Mo(bpy)(CO)$_4$ As Revealed by Vibrational Sum-Frequency Generation Spectroscopy, *J. Am. Chem. Soc.*, 2017, **139**, 13791–13797.

155 M. Bourrez, *et al.*, Pulsed-EPR evidence of a manganese(II) hydroxycarbonyl intermediate in the electrocatalytic reduction of carbon dioxide by a manganese bipyridyl derivative, *Angew. Chem., Int. Ed.*, 2014, **53**, 240–243.

156 M. Stanbury, J.-D. Compain and S. Chardon-Noblat, Electro and photoreduction of CO_2 driven by manganese-carbonyl molecular catalysts, *Coord. Chem. Rev.*, 2018, **361**, 120–137.

157 D. C. Grills, M. Z. Ertem, M. McKinnon, K. T. Ngo and J. Rochford, Mechanistic aspects of CO_2 reduction catalysis with manganese-based molecular catalysts, *Coord. Chem. Rev.*, 2018, **374**, 173–217.

158 Y. C. Lam, R. J. Nielsen, H. B. Gray and W. A. Goddard, A Mn Bipyrimidine Catalyst Predicted To Reduce CO_2 at Lower Overpotential, *ACS Catal.*, 2015, **5**, 2521–2528.

159 C. Riplinger and E. A. Carter, Influence of Weak Brønsted Acids on Electrocatalytic CO_2 Reduction by Manganese and Rhenium Bipyridine Catalysts, *ACS Catal.*, 2015, **5**, 900–908.

160 M. Bourrez, F. Molton, S. Chardon-Noblat and A. Deronzier, [Mn(bipyridyl)(CO)$_3$Br]: an abundant metal carbonyl complex as efficient electrocatalyst for CO_2 reduction, *Angew. Chem., Int. Ed.*, 2011, **50**, 9903–9906.

161 A. J. Cowan, Water oxidation: intermediate identification, *Nat. Chem.*, 2016, **8**, 740–741.